

---

# Spectropolarimetry of the superwind filaments of the starburst galaxy M82 II: kinematics of the dust surrounding the nuclear starburst

Michitoshi YOSHIDA<sup>1,2</sup> \*, Koji S. KAWABATA<sup>2</sup>, Youichi OHYAMA<sup>3</sup>,  
Ryosuke ITOH<sup>4,5</sup> and Takashi HATTORI<sup>1</sup>

<sup>1</sup>Subaru Telescope, 650 North A'ohoku Place, Hilo, Hawaii 96720, U.S.A.

<sup>2</sup>Hiroshima Astrophysical Science Center, Hiroshima University, Hiroshima 739-8526, Japan

<sup>3</sup>Academia Sinica, Institute of Astronomy and Astrophysics, 11F of AS/NTU, Astronomy-Mathematics Building, No. 1, Sec. 4, Roosevelt Rd., Taipei 10617, Taiwan, R.O.C.

<sup>4</sup>Department of Physical Science, Hiroshima University, Hiroshima 739-8526, Japan

<sup>5</sup>Department of Physics, Tokyo Institute of Technology, Meguro-ku, Tokyo 152-8551, Japan

\*E-mail: yoshida@naoj.org

Received ; Accepted

## Abstract

We performed deep spectropolarimetric observations of a prototypical starburst galaxy M82 with the Subaru Telescope in order to study the kinematics of the dust outflow. We obtained optical polarized emission-line spectra up to  $\sim 4$  kpc away from the nucleus of the galaxy along three position angles,  $138^\circ$ ,  $150^\circ$  and  $179^\circ$  within the conical outflowing wind (superwind). The  $H\alpha$  emission line in the superwind is strongly polarized and the polarization pattern shows dust scattering of central light sources, being consistent with the previous works. The intensity weighted polarization degree of the  $H\alpha$  line reaches  $\sim 30\%$  at maximum. There are at least two light sources at the central region of the galaxy; one of which is located at the near-infrared nucleus and the other resides at one of the peaks of the 3 mm radio and molecular gas emission. The outer ( $> 1$  kpc) dust is illuminated by the former, whereas the inner dust is scattering the light from the latter. We investigated as well the dust motion from the velocity field of the polarized  $H\alpha$  emission line. The dust is accelerated outward on the northwest side of the nucleus. A simple bi-conical dust outflow model shows that the outflow velocity of the dust reaches  $\gtrsim 300 - 450$  km s<sup>-1</sup> at  $\sim 4$  kpc from the nucleus, suggesting that some portion of the dust escapes from the gravitational potential of M82 into the intergalactic space. At some regions on the southeast side, in particular along the position angle of  $138^\circ$ , the dust has radial velocity slower than the systemic velocity of the galaxy, apparently suggesting inflowing motion toward the nucleus. These components are spatially consistent with a part of the molecular gas stream, which is kinematically independent of the outflow gas, thus the apparent inflow motion of the dust reflects the streaming motion associated with the molecular gas stream.

**Key words:** galaxies:individual(M82) — galaxies:nearby — galaxies:starburst — interstellar:dust

---

## 1 Introduction

Large scale gas outflows are ubiquitous phenomena seen in active star-forming galaxies (Martin et al. 2012; Chisoml et al. 2015; Heckman & Thompson 2017). The most energetic class of these flows is called “superwind” associated with starburst (Heckman, Armus & Miley 1990; Heckman 2003; Veilleux, Cecil & Bland-Hawthorn 2005). A superwind expels much of the interstellar medium out of the galaxy disk, contributing the heating and metal pollution of the galactic halo and the intergalactic space, as well as quenching the star formation activity in the galaxy (Aguirre et al. 2001a; Aguirre et al. 2001b; Adelberger et al. 2003). The latter effect, so called the “feedback” of galaxy star formation, has been thought as one of the most important processes in the galaxy evolution (Croton et al. 2006; Peebles & Shankar 2011; Hopkins, Quataert & Murray 2012; Faucher-Giguère, Quataert & Hopkins 2013).

In spite of this importance, the detailed physical mechanisms that drive a superwind have not been fully understood yet. The trigger and energy source of a superwind are newly born massive stars and supernova explosions inside starburst regions. The collective effect of stellar winds and supernovae initiates a superwind (Chevalier & Clegg 1985; Suchkov et al. 1994; Tenorio-Tagle & Muñoz-Tuñón 1998; Strickland & Stevens 2000; Cooper et al. 2008). There are several different physical models for driving superwind; thermal pressure driven wind (Chevalier & Clegg 1985; McClow, McCray & Norman 1989; Fujita et al. 2009), ram pressure driven wind (Cooper et al. 2008; McCourt et al. 2015), and radiation pressure driven wind (Murray, Ménard & Thompson 2011; Ostriker & Shetty 2011; Hopkins, Quataert & Murray 2012; Krumholz & Thompson 2012; Krumholz & Thompson 2013; Thompson & Krumholz 2016; Zhang et al. 2018).

The radiation pressure has been thought to be one of the most efficient mechanisms to launch and accelerate stellar wind (Spitzer 1978; Murray, Ménard & Thompson 2011). In the case of stellar wind, circumstellar dust is pushed and accelerated outward by the radiation pressure of the central star light (Spitzer 1978). The neutral gas hydrodynamically coupled with the dust is dragged by the dust and accelerated outward, and a strong dusty gaseous wind is formed.

In galactic scale, radiation pressure can affect the global gas dynamics of the galaxy interstellar medium (Thompson et al. 2015; Zhang et al. 2018). In particular, strong emission from massive star clusters or starburst regions can drive a large scale galactic wind via radiation pressure

as in the case of stellar wind. One of the key ingredients of the radiation pressure-driven wind is dust. Large opacity of dust to ultraviolet light enables a dust grain catch strong pressure force from the radiation illuminating it (Murray, Ménard & Thompson 2011; Ostriker & Shetty 2011; Hopkins, Quataert & Murray 2012; Davis et al. 2014; Thompson et al. 2015; Thompson & Krumholz 2016; Zhang & Davis 2017; Zhang et al. 2018). Several model calculations have predicted that dust can be accelerated over the escape velocity of a galaxy (Ferrara et al. 1991; Murray, Ménard & Thompson 2011; Zhang et al. 2018).

It has been well known that starburst superwind is highly dusty in general (Scarrott, Eaton & Axon 1991; Ichikawa et al. 1994; Alton, Davies & Bianchi 1999; Leeuw & Robson 2009; Kaneda et al. 2010). The dust embedded in the galactic disk or newly formed in the starburst region is entrained by the hot gas outflow or pushed directly by the radiation pressure from the starburst driving a dusty neutral gas outflow (Heckman et al. 2000; Martin 2005; Rupke, Veilleux & Sanders. 2005; Heckman et al. 2015). Revealing the kinematics of dust outflow and its relationship with the motions of the other species gives us an important clue to understanding the structure and dynamics of the outflow and hence the physics of radiation pressure driven wind.

M82 is a intensively studied nearby starburst galaxy with a remarkable superwind. Its proximity (3.89 Mpc; Sakai & Madore 1999) allows us to investigate in detail the starburst activity and its relationship with the superwind. Many observational studies have been done for the superwind of this galaxy (Bland & Tully 1988; Heckman, Armus & Miley 1990; Brouillet & Schilke 1993; Bregman, Schulman & Tomisaka 1995; Shopbell & Bland-Hawthorn 1998; Kaaret et al. 2001; Ohyama et al. 2002; Hoopes et al. 2005; Engelbracht et al. 2006; Tsuru et al. 2007; Strickland & Heckman 2009; Leeuw & Robson 2009; Veilleux, Rupke & Swaters 2009; Westmoquette et al. 2009; Kaneda et al. 2010; Contursi et al. 2013; Salak et al. 2013; Salas et al. 2014; Bierão et al. 2015; Leroy et al. 2015). The superwind of M82 is well known to be highly dusty. Optical-infrared imaging observations revealed a complex structure mixed with dust and ionized gas near the galaxy disk (Ichikawa et al. 1994; Ohyama et al. 2002). Sub-mm, mid-infrared and far-infrared observations detected emission from the dust associated with the superwind (Alton, Davies & Bianchi 1999; Engelbracht et al. 2006; Leeuw & Robson 2009; Kaneda et al. 2010; Leroy et al. 2015). Optical imaging polarimetry and UV observations made it clear that the nuclear starburst emission is scattered by the dust in the superwind (Scarrott, Eaton & Axon

\* Based on data collected with the Subaru Telescope operated by the National Astronomical Observatory of Japan

1991; Hoopes et al. 2005). Although these observations revealed that huge amount of dust is associated with the superwind, the kinematics of the dust has not been well known.

Yoshida, Kawabata & Ohya (2011), YKO11 investigated the motion of the dust in the superwind of M82 by means of spectropolarimetry of the  $H\alpha$  emission. Their idea is very simple; the dust in the wind scatters and polarizes the strong  $H\alpha$  emission from the nuclear starburst region, i.e., the dust grains act as “moving mirrors”. Hence the observed velocity of the polarized  $H\alpha$  line reflects the motion of the dust. YKO11 found that the outflow velocity of the dust in the M82 superwind decelerates outward from the nucleus and the dust outflow almost stops around 1 kpc from the nucleus. The spatial coverage of their observation was, however, too limited to derive the global kinematics of the dust flow.

Here we report the results of our further optical spectropolarimetric observation of M82 in order to study the dust kinematics of the superwind through polarized  $H\alpha$  emission. Our new observation is much wider and deeper than the observation of YKO11, reaching  $\sim 4$  kpc from the nucleus along three position angles.

We adopted 3.89 Mpc as the distance to M82 (Sakai & Madore 1999), which yields a linear scale of  $18.9 \text{ pc arcsec}^{-1}$  for the galaxy. The heliocentric systemic velocity ( $v_{\text{sys}}$ ) we used in this paper is  $203 \text{ km s}^{-1}$  (Götzt et al. 1990; Shopbell & Bland-Hawthorn 1998).

## 2 Observation

We performed spectropolarimetric observations of M82 with FOCAS (Kashikawa et al. 2002), attached to the Cassegrain focus of the Subaru Telescope (Kaifu et al. 2000; Iye et al. 2004), on January 16 and 17, 2013 UT. The observations were carried out using the spectropolarimetric mode of FOCAS (Kawabata et al. 2003). We used a slit mask with eight  $0''.8$  (width)  $\times$   $20''.6$  (length) slitlets at  $23''.7$  intervals, and a VPH grism with  $665 \text{ grooves mm}^{-1}$  whose central wavelength is  $6500 \text{ \AA}$  (Ebizuka et al. 2011). The resultant spectral resolving power was  $\lambda/\Delta\lambda \approx 1700$ , determined by the combination of the slit and the grating. The separation direction of the beam splitting by the Wollaston prism was parallel to the direction of the slit length, and spectra of both ordinary and extraordinary rays were obtained simultaneously. We made 4 pixel binning of the CCD along the slit, which resulted in a spatial sampling of  $0''.4$  per pixel.

The position angles (PAs) of the slit were set at  $138^\circ$ ,  $150^\circ$ , and  $179^\circ$  (hereafter, referred as to PA 138, PA 150, and PA 179, respectively). Figure 1 shows the positions

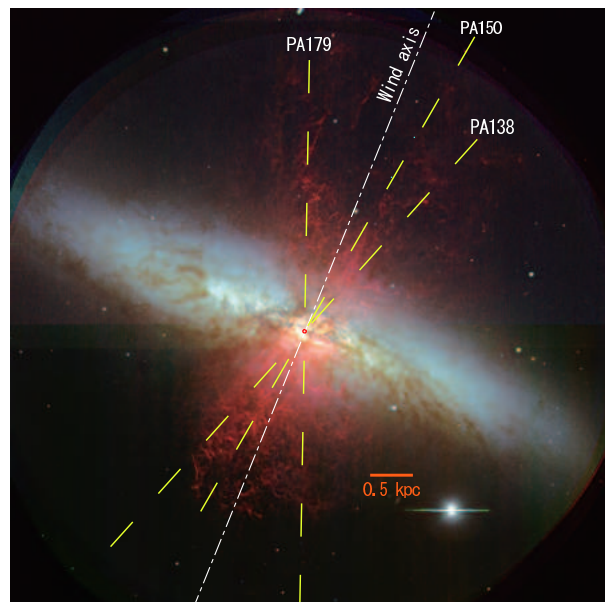


**Fig. 1.** The slit positions overlaid on the  $B$  (blue),  $V$  (green), and  $H\alpha$  (red) pseudo color image of M82. The image was reproduced from the image in the Subaru Telescope website.

of the slits overlaid on an image of M82 taken from the Subaru Telescope website<sup>1</sup>. We assumed the position of the  $2.2 \mu\text{m}$  nucleus (Dietz et al. 1989; Telesco et al. 1991) as the center of the galaxy (the origin of the coordinates shown in the figures in this paper is set at this position). One polarimetry unit data set consists of exposures taken at four different angles ( $0^\circ$ ,  $22.5^\circ$ ,  $45^\circ$ , and  $67.5^\circ$ ) of the half-wave plate. The exposure time is 600 sec per one half-wave plate angle; it took  $4 \times 600 \text{ s}$  to obtain one data set. We obtained three data sets for PA 138 and PA 150, and four data sets for PA 179. Thus, the total exposure times were 1800 sec per one half-wave plate angle for PA 138 and PA 150 and 2400 sec for PA 179 (Table 1).

We observed an unpolarized star HD 18803 and a strongly polarized star HD 43384 to calibrate the polarization. Using HD 18803, we mapped the instrumental polarization along the slit by making spectropolarimetry of the star through all the eight slitlets. We observed a spectrophotometric standard star Feige 110 as well. Both the observing nights were clear and the seeing was approximately  $0''.8$  in the first night and  $0''.7\text{--}1''.0$  in the second night.

## 3 Data Reduction

Standard CCD data reduction was applied to the raw CCD frames using IRAF. The overscan level was subtracted from all frames. All the bias frames taken in the observing

<sup>1</sup> <https://subarutelescope.org/Pressrelease/2000/03/24/index.html>

**Table 1.** The observing log of the spectropolarimetry of M82

Date (UT)	Object	PA [degree]	Exp.Time [sec]
2013-01-16	M82	150	3×4×600
	M82	138	3×4×600
	HD 18803	90	8×4×10
	HD 43384	90	4×10
2013-01-17	M82	179	4×4×600
	HD 43384	90	4×10

run were averaged and the averaged bias frames were subtracted from the object and dome flat frames. Since the dark current was negligible ( $< 1$  ADU), dark subtraction was not performed. Flat fielding was carried out using the dome flat frames averaged over the four PAs of the half-wave plate. Image distortion was corrected by the “distcalib” task of “FOCASRED” package which is an IRAF package dedicated to the data reduction of FOCAS. The frames of the same PA were coadded by taking median of the frames.

We extracted eight sets of two-dimensional spectra of ordinary and extraordinary rays for each PA data. Then the two-dimensional wavelength calibration was done for each spectrum using sky emission lines. In order to perform sky subtraction, we first created the two-dimensional sky spectra from the spectra taken with the most outer slitlet for each PA. However, faint  $H\alpha$  emission lines were observed even in the most outer region spectra. Hence we carefully compared the spectra of the wavelength region from  $6500 \text{ \AA}$  to  $6600 \text{ \AA}$  of the most outer region of the M82 data with the pure sky spectra taken by another galaxy observation in the same night. Then we extracted the differences between these two spectra and confirmed if the residuals corresponded to  $H\alpha$ + $[N \text{ II}]$  complex, and subtracted these residuals from the most outer region spectra of M82. We subtracted these final sky spectra from all the object spectra.

We selected bright spots or blobs of the  $H\alpha$  emission in the two dimensional spectra by eye-inspection. The areas of the selected regions are shown in Table 2 in Appendix 2. The polarization parameters were calculated from the one-dimensional spectra (ordinary and extraordinary at the four wave-plate PAs) employing the method described in section 6.1.2 of Tinbergen (1996). Our observations of unpolarized star HD 18803 indicated that instrumental polarization was negligible ( $\lesssim 0.1\%$ ) over the field-of-view. Moreover, our measurements of flat-field lamps through fully polarizing filters showed that the depolarization factor was also negligible ( $\lesssim 0.05$ ). Therefore, we made no correction for instrumental polarization and depolarization.

The zero point of the polarization position angle on the sky was determined from the observation of the strongly polarized star HD 43384. The total and polarized spectra in the wavelength region of  $H\alpha$ + $[N \text{ II}]$  emission lines are shown in Appendix 1. The error estimation of the polarization parameters was performed using the method described in Kawabata et al. (1999).

We fitted Gaussian profiles to the emission line spectra for both the total light and the polarized light. First we applied Gaussian fitting to the  $H\alpha$ + $[N \text{ II}]$  spectra, assuming that  $H\alpha$ ,  $[N \text{ II}]\lambda 6548$ , and  $[N \text{ II}]\lambda 6583$  have the same radial velocities and full widths at half maximum (FWHMs). We fixed the emission line intensity ratio  $[N \text{ II}]\lambda 6583/\lambda 6548$  at 3 in this procedure. Most of the  $H\alpha$ + $[N \text{ II}]$  emission lines both in total light and polarized light have asymmetric profile, some of which exhibit double-peaked profile (see figures in Appendix 1). We fitted multiple Gaussian profiles to these  $H\alpha$ + $[N \text{ II}]$  lines to decompose their asymmetric profiles. The radial velocities and FWHMs of the  $H\alpha$ + $[N \text{ II}]$  lines of one kinematic component were assumed to be the same for the decomposition. We also fitted single Gaussian fitting to the emission line profiles to derive intensity-weighted velocities of the emission lines.

We applied the same procedure for measuring  $[S \text{ II}]\lambda\lambda 6717/6731$  doublet. In this case, we took the emission line intensity ratio  $[S \text{ II}]\lambda 6731/\lambda 6717$  as a free parameter in fitting the emission line profiles.

## 4 Results

We summarized the results of our polarization data reduction in Table 2 in Appendix 2. In the following subsections, we describe the characteristics of the polarization vectors and velocity field of the  $H\alpha$  emission of the M82 superwind.

### 4.1 Polarization vectors of the $H\alpha$ emission

#### 4.1.1 Global pattern

Figure 2 shows the intensity weighted polarization vectors of the  $H\alpha$  emission of M82. The polarization data taken by YKO11 (five polarization vectors along PA  $150^\circ$  and three polarization vectors along PA  $134^\circ$ ) are also shown in this figure. The distribution of the polarization vectors is circularly symmetric, indicating that the polarized light is the scattering/reflecting light of central compact bright sources. A closeup view of the central region of the galaxy is shown in Figure 3. This result is consistent with the previous works (Scarrott, Eaton & Axon 1991; YKO11). Our data are overplotted on the  $H\alpha$  imaging polarization map of Scarrott, Eaton & Axon (1991) in Figure 4. Both results show very good agreement in the inner region, and our ob-



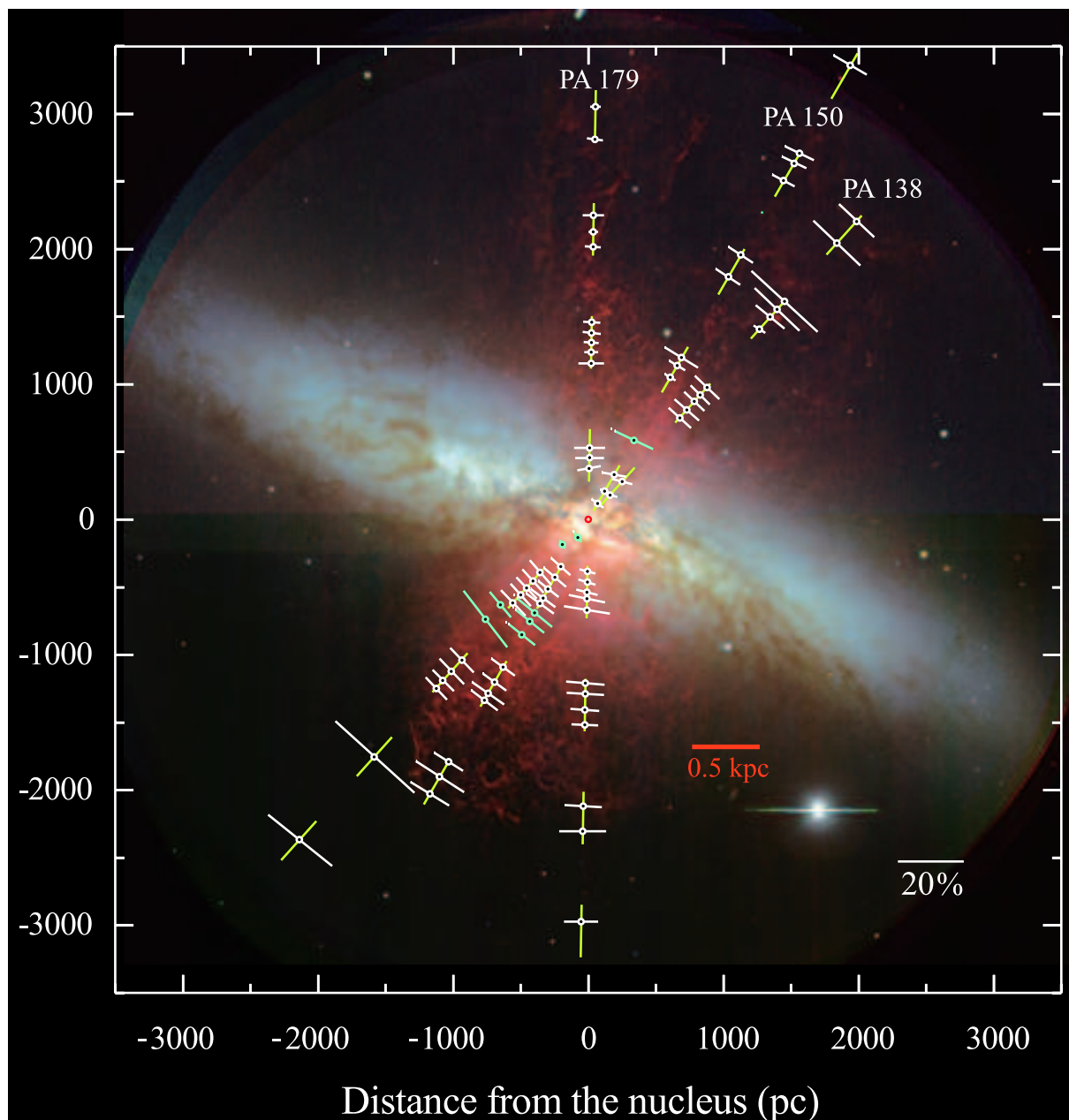


**Fig. 2.** Polarization vectors of the  $H\alpha$  emission of M82 overlaid on Figure 1. The origin of the coordinates is set at the position of the  $2.2\ \mu\text{m}$  nucleus (Dietz et al. 1989; Telesco et al. 1991). White lines represent the polarization vectors obtained in this work. Light blue lines show the data obtained by YKO11.

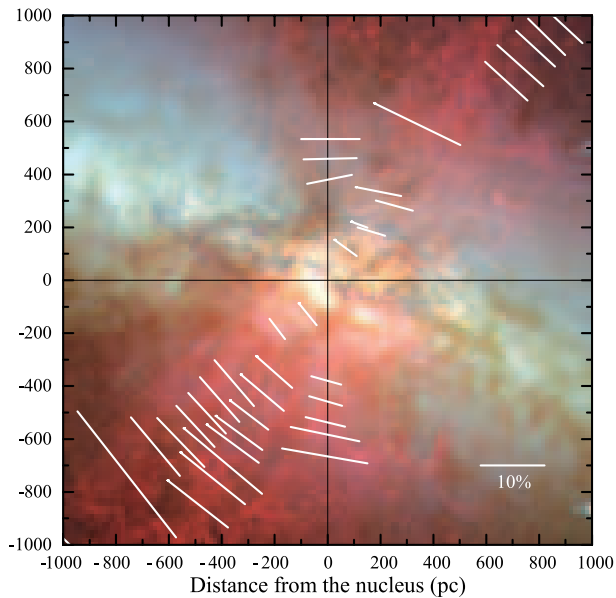


Fig. 3. Same as Figure 2, but for the central part of the galaxy.

servation revealed that the circular symmetric pattern of the polarization vectors is maintained to more than twice larger distance,  $\sim 4$  kpc from the nucleus, than the  $H\alpha$  map of Scarrott, Eaton & Axon (1991). At the faint end of the  $H\alpha$  nebula along PA 138, the  $H\alpha$  lines are strongly polarized (Figures 2 and 4). Extension of the polarized  $H\alpha$  is comparable to that of the scattered UV emission observed with *GALEX* (Hoopes et al. 2005).

There is a tendency that the polarization degree is larger as the distance from the nucleus is larger. Some parts of the outer nebula show the polarization degree as large as  $\sim 30\%$  (Figure 5). This means that a significant fraction of the  $H\alpha$  emission in the outer region of the superwind of M82 is scattered light.

#### 4.1.2 Central illumination sources

There are at least two possible main illumination sources, which are strong  $H\alpha$  emitting regions, in the nuclear region of M82. The polarization magnetic field vectors (hereafter referred as to “M vectors”), which are perpendicular to the polarization electric vectors and indicate the directions of illumination sources, in the central region of M82 are shown in Figure 6. Most of the M vectors within 1 kpc from the nucleus converge at a region located about  $6''$  ( $\sim 100$  pc) west from the  $2.2\ \mu\text{m}$  nucleus (a red circle in Figure 6), suggesting that the main illumination source for the central part of the  $H\alpha$  nebula is located here. This is again consistent with the results of Scarrott, Eaton & Axon (1991). The light source of the scattered  $H\alpha$  in the central 1 kpc region must be deeply embedded in the dust clouds around the nucleus, because there is no bright fea-

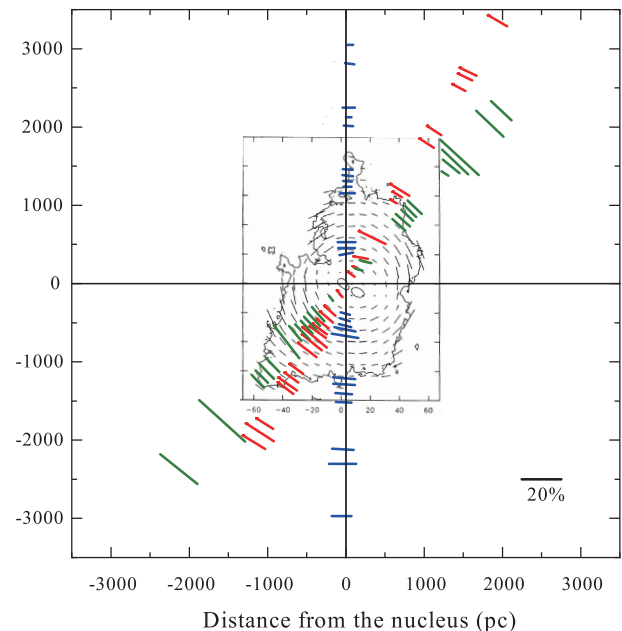


Fig. 4. Polarization vectors of the  $H\alpha$  emission of M82 obtained in this work overlaid on the polarization map of Scarrott, Eaton & Axon (1991). Green, red, and blue colored lines represent the polarization vectors along PA 138, PA 150, and PA 179, respectively.

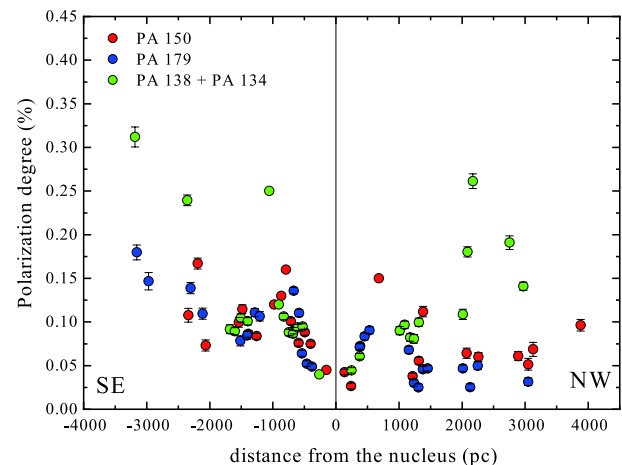
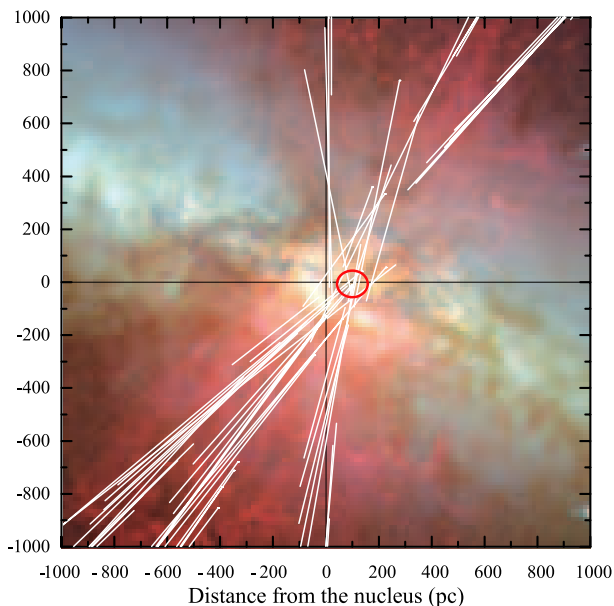


Fig. 5. Polarization degrees of the  $H\alpha$  emission of M82 plotted against the distance from the nucleus. The polarization degrees increase with the distance.



**Fig. 6.** The magnetic field vectors (M vectors) of the  $H\alpha$  emission, which represent the direction to the light sources of the scattering of the nebula, in the central region of M82. The red circle indicates the converging position of the M vectors within 1 kpc from the nucleus.

ture indicating intensive star-formation in optical. The position of this light source coincides very well with that of a peak of the nuclear 3 mm radio emission (Salas et al. 2014; Ginard et al. 2015) and a molecular gas concentration (Walter, Weiß & Scoville 2002; Salas et al. 2014; Ginard et al. 2015) (Figure 7). This 3 mm peak is thought to be an active star forming region located at the east edge of the molecular gas superbubble (Matsushita et al. 2005; Weiß, Walter & Scoville 2005; Ginard et al. 2015; Chisholm & Matsushita 2016).

Detailed investigation of the polarization pattern shows that the inner 2 kpc part of the SE wind is preferentially illuminated by this western offset source (left panel of Figure 8). A part of the inner 500 pc region of the NW wind is also illuminated by this offset source. On the other hand, most other part on the NW side of the nucleus and the outer region on the SE side of the nucleus are illuminated by the region around the  $2.2 \mu\text{m}$  nucleus (right panel of Figure 8). The fraction of which source is dominant for the scattered light would be determined by the spatial configuration of the light sources and the intervening dust.

We investigated the intensity ratios of the polarized emission lines to examine the nature of the scattered light source. Figure 9 shows the emission line intensity ratios of  $[\text{N II}]\lambda 6583/H\alpha$  to  $[\text{S II}]\lambda\lambda 6713 + 6731/H\alpha$  (hereafter referred as to  $[\text{N II}]/H\alpha$  and  $[\text{S II}]/H\alpha$ , respectively) of the M82 superwind in both total and polarized lights. We found that the two line intensity ratios of the total light

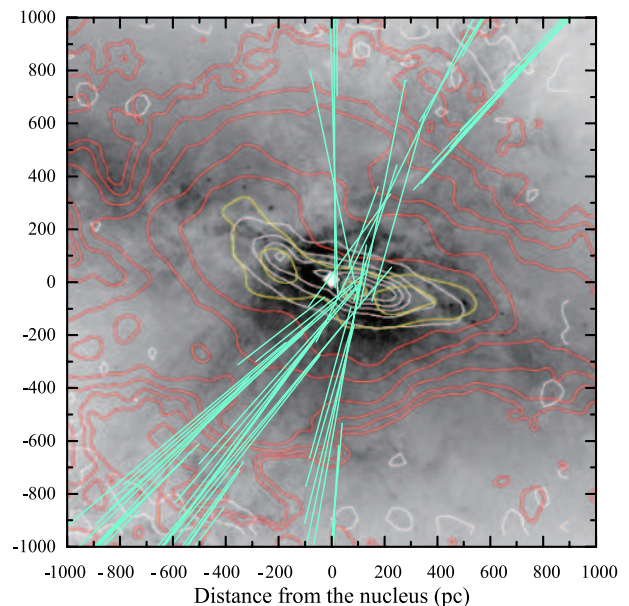


**Fig. 7.** Scattering directions of the  $H\alpha$  emission in the central region of M82 overlaid on radio images. The white, red, and yellow contours represent 3 mm continuum emission (Salas et al. 2014), outflow component of CO  $J = 1-0$  emission, and molecular disk component of CO  $J = 1-0$  (Walter, Weiß & Scoville 2002), respectively. The white rhombus indicates the position of the  $2.2 \mu\text{m}$  nucleus. The background gray scale is a  $H\alpha$  image taken with *HST*/ACS (Mutchler et al. 2007).

tightly and positively correlate to each other. This can be explained by a simple model in which a fraction of the emission lines from shock-heated ionized gas showing enhanced forbidden lines of  $[\text{N II}]$  and  $[\text{S II}]$  changes with respect to those from the ionized gas photoionized by massive stars. Similar trend has been reported by, e.g., McCarthy, Heckman & van Breugel (1987). On the other hand, the polarized emission line intensity ratios are almost constant,  $\log([\text{N II}]/H\alpha) \simeq -0.28$  and  $\log([\text{S II}]/H\alpha) \simeq -0.52$ , over a range of distance from the nucleus. As pointed out by YKO11, these line intensity ratios are almost equal to those of the nuclear region (Westmoquette et al. 2009). Note that our slitlets did not cover the nuclear region of M82 (see Figure 1). The  $[\text{S II}]/H\alpha$  is larger in the total light than in the polarized light in most regions. All these properties support an idea that the emission from the nuclear region is scattered and seen as the polarized emission in addition to the shock-heated local emission seen in total light from the extended wind. Some outlying data points showing smaller  $\log([\text{S II}]/H\alpha) \sim -0.9$  in the polarized emission line may be caused by additional scattered light contribution from local low-excitation light sources outside the nucleus.

We derived the electron density  $n_e$  from the intensity ratio of  $[\text{S II}]\lambda 6731/\lambda 6717$  assuming the ionized gas temperature of  $10^4$  K (Osterbrock & Ferland 2006). The  $n_e$  obtained from the total light decreases with distance

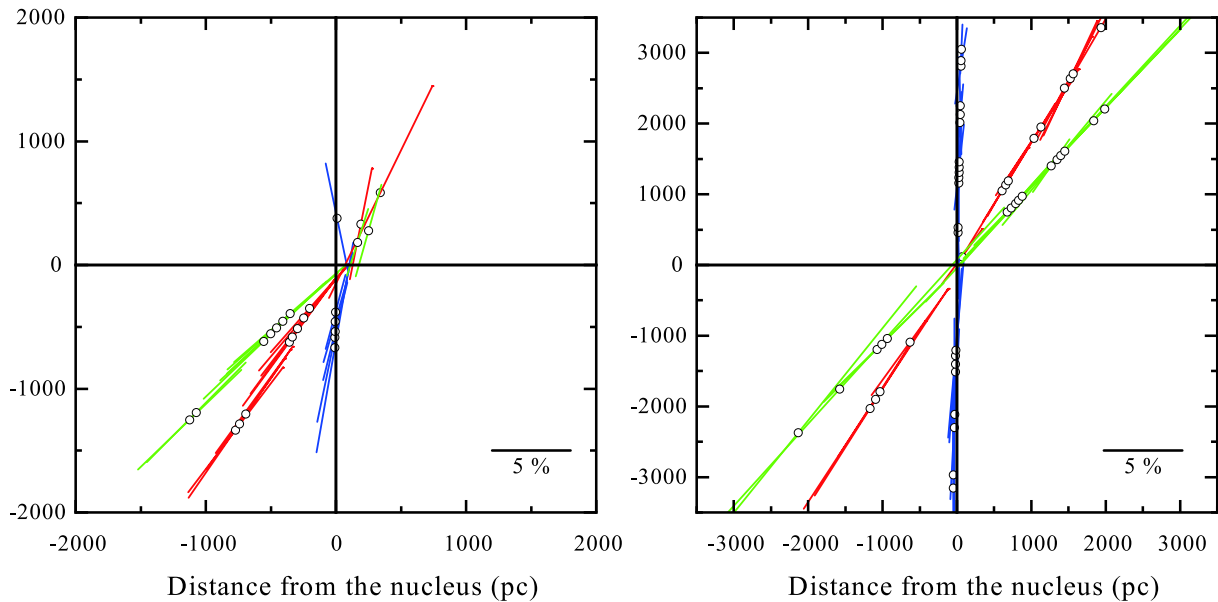


**Fig. 8.** The scattering directions (the M vectors) of the  $H\alpha$  emission of M82. Left: the M vectors converged around the position of the 3 mm radio emission peak. Right: the vectors converged around the  $2.2 \mu\text{m}$  nucleus. Note that the spatial scales are different between the two panels.

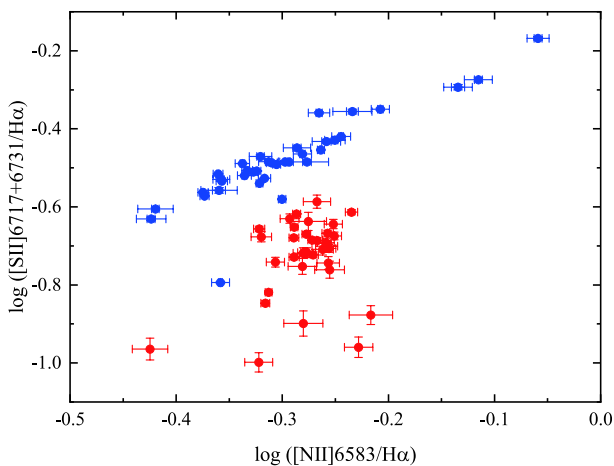


**Fig. 9.** Emission line intensity ratio diagram of  $\log([N \text{ II}]\lambda 6583/H\alpha)$  vs.  $\log([S \text{ II}]\lambda\lambda 6713+6731/H\alpha)$  of the total light (blue dots) and polarized light (red dots) of the superwind of M82.

from the nucleus, and is less than  $100 \text{ cm}^{-3}$  beyond 1 kpc (Figure 10). On the other hand,  $n_e$  derived from the polarized emission lines is almost constant at  $500\text{--}1000 \text{ cm}^{-3}$ . Similar results were obtained by YKO11 over limited area. It is known that the ionized gas in the nuclear star-forming regions shows such higher electron density (e.g., Heckman, Armus & Miley 1990). All these properties can be explained in a model where we measure the density of the light source at the nucleus seen in a scattered light over an extended wind. Taking a closer look, we noted that the  $n_e$  derived from the polarized light is slightly smaller beyond 1 kpc from the nucleus. This might indicate that

the light sources of the scattered light in the inner and outer regions are different, as we noted earlier based on the polarization angles. If this is the case, the electron density at the 3 mm nucleus is larger than that of the  $2.2 \mu\text{m}$  nucleus. However, as mentioned above regarding sudden change of  $\log([N \text{ II}]/H\alpha)$  and  $\log([S \text{ II}]/H\alpha)$ , there is a possibility that local light sources outside the nucleus showing low-excitation spectra from low electron density ionized gas can contribute to the observed polarized emission. Such contaminating light sources can also explain relatively higher  $n_e$  ( $\sim 5000 \text{ cm}^{-3}$ ) at  $\sim 1.3 \text{ kpc}$  if such sources have denser ionized gas. Given such possible contaminating light sources outside the nucleus, we attribute the electron density  $n_e \sim 10^3 \text{ cm}^{-3}$  derived in the inner  $< 1 \text{ kpc}$  region with the polarized scattered light to that of the central scattering light source.

#### 4.1.3 Local structure probed by polarization angle change in emission line profile

In some inner regions, significant changes in polarization angle within the profile of an emission line are observed (see Figures 28–36 in Appendix 1 for example). Some of such regions seem to be caused by poor signal-to-noise ratio, whereas there are several definite cases of real rotation of the polarization vector in the profiles of the polarized emission lines. The most prominent case is the spectrum at 0.38 kpc SE from the nucleus at PA 179 (Figure 11; we refer this position as to P1). The main part of the  $H\alpha$  line shows a polarization angle of  $\sim 75^\circ$ . There is an additional weak, blue-shifted narrow component whose radial



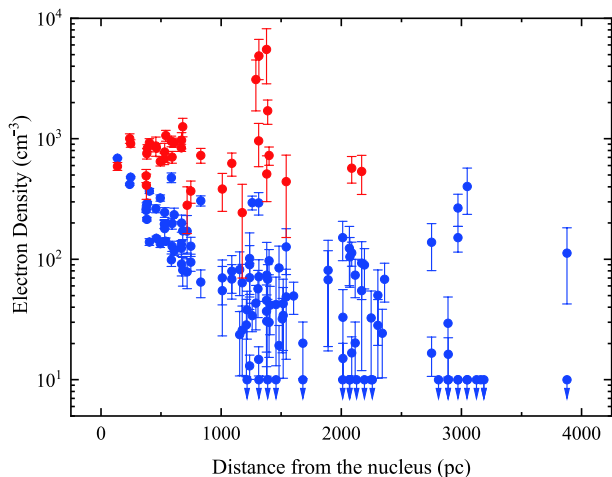


**Fig. 10.** Electron densities  $n_e$  derived by  $[\text{S II}]\lambda 6731/[\text{S II}]\lambda 6717$  emission line intensity ratios. Blue and red dots represent  $n_e$  derived by the total light and by the polarized light, respectively.

velocity is about  $\sim 90 \text{ km s}^{-1}$  in the  $\text{H}\alpha + [\text{N II}]$  emission (indicated by arrows in Figure 11). The PA of the polarization vector abruptly changes around this blue-shifted component, reaching  $\sim 180^\circ$  at the peak of the blue-shifted emission lines. Intensity-weighted polarization angle of the blue-shifted component is  $\sim 170^\circ$ . The  $\text{H}\alpha$  lines at 0.14 kpc NW at PA 150 (P2) and 0.25 kpc NW at PA 138 (P3) also show clear polarization angle changes (Figures 12 and 13). At P2, the polarization angle changes from  $\sim 25^\circ$  to  $\sim 75^\circ$  in the emission line profile from blue to red (Figure 12). At P3, the polarization angles of the blue side and the red side of the  $\text{H}\alpha$  line are  $\sim 95^\circ$  and  $\sim 40^\circ$ , respectively (Figure 13).

The polarization angle variations of the inner regions described above are summarized in Figure 14. We plot the M vectors of the polarized light on an X-ray image taken by *Chandra* (Kaaret et al. 2001). The M vectors of the red components of the polarized  $\text{H}\alpha$  at P2 and P3 are almost directed to the  $2.2 \mu\text{m}$  nucleus, suggesting the scattered light source of these scattered components is this nucleus. On the other hand, the M vector of the red component at P1 suggests that the light source is the 3 mm peak (Figure 14).

The blue components of the polarized  $\text{H}\alpha$  at these positions show different behavior. We could not identify their candidate light sources in optical band. There is, however, a faint X-ray point source that lies in the direction of the M vector of the blue component at P1, suggesting a possibility that the X-ray source is the light source of this component. For P3, the M vector of the blue component is roughly directed to a bright X-ray source (X41.4+60 (Kaaret et al. 2001) or M82 X1 (Matsumoto et al. 2001; Bachetti et al. 2014)). The blue components of the polarized  $\text{H}\alpha$  are pos-

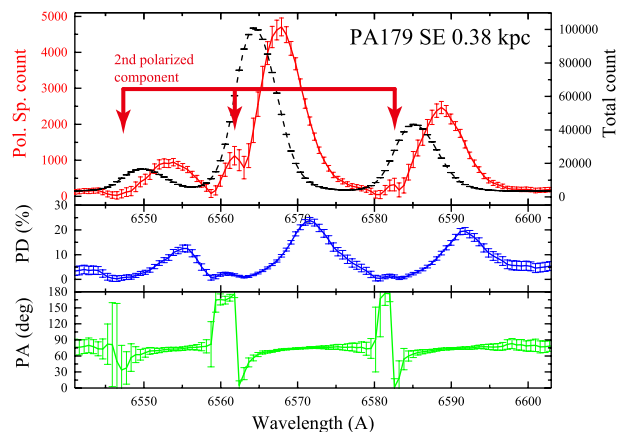


**Fig. 11.** The polarization spectrum of  $\text{H}\alpha + [\text{N II}]$  emission lines at 0.38 kpc SE from the nucleus along PA 179 (P1). Top panel: the polarized light (red solid line) and total light spectra (black dashed line). Middle panel: the polarization degree. Bottom panel: the polarization angle. A secondary velocity component is clearly seen in the polarized spectrum (arrows indicate  $\text{H}\alpha + [\text{N II}]$  complex of the secondary component). It is remarkable that there is a large change of the polarization angle at the peaks of the secondary emission line component.

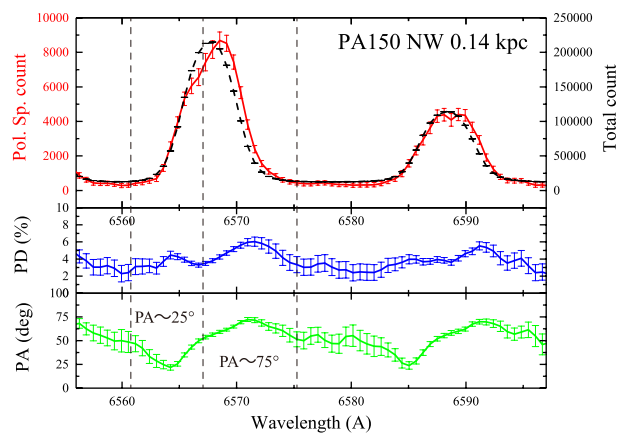


**Fig. 12.** The polarization spectrum of  $\text{H}\alpha + [\text{N II}]\lambda 6583$  emission lines at 0.14 kpc NW from the nucleus along PA 150 (P2). The configuration of the figure is the same as Figure 11. The polarization angle shows a significant change near the peak of the profile of the total light emission lines; the polarization angle at the blue side of the emission line is  $\sim 25^\circ$ , whereas that at the red side is  $\sim 75^\circ$ .

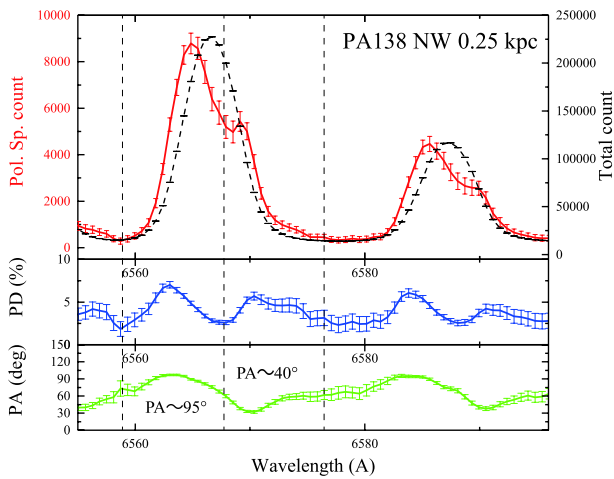


**Fig. 13.** The polarization spectrum of  $H\alpha$ + $[N II]\lambda 6583$  emission lines at 0.25 kpc NW from the nucleus along PA 138 (P3). The configuration of the figure is the same as Figure 11. There is a dip at the red side of the polarized emission line profile. Both of the polarization degree and polarization angle changes are seen at the dip position.

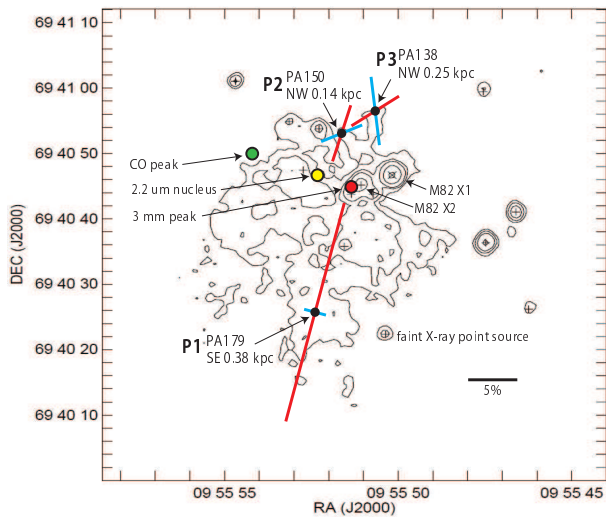


**Fig. 14.** The M vectors of the polarized  $H\alpha$  emission lines that show significant polarization angle change in the profiles (P1–3) are plotted on a soft X-ray map taken with *Chandra* (Kaaret et al. 2001). Blue and red straight lines correspond blue and red components, respectively, of the polarized emission lines. The M vector of the blue component at P1 is directed to a faint X-ray source located west of P1. The M vector of the blue component at P3 is roughly directed to the brightest X-ray point source of the galaxy, M82 X-1 (Matsumoto et al. 2001; Bachetti et al. 2014).

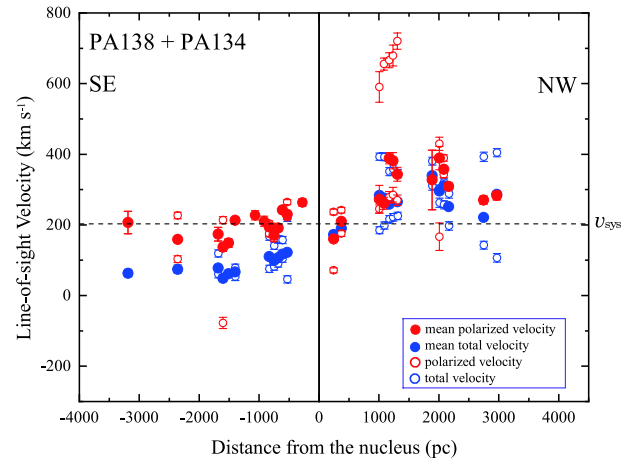


**Fig. 15.** The velocity field of the  $H\alpha$  emission lines along PA=138° and 134°. The data of PA=134° are taken from YKO11. The open circles show the velocities derived from multiple-component fitting of the emission lines. The filled circles represent intensity-weighted mean velocities. Red circles are the data of the polarized light. Blue circles are the data of the total light. The systemic velocity of the galaxy,  $v_{\text{sys}} = 203 \text{ km s}^{-1}$ , is shown by a dotted line.

sibly the scattered light of these sources. The M vectors of the blue component of P2 and the red component of P3 have similar position angles, roughly pointing to the western peak of the central molecular disk (Figure 7).

## 4.2 Velocity field of the polarized $H\alpha$ line

### 4.2.1 Global velocity field

We derived the velocity field of the  $H\alpha$  of the total light and the polarized light. Figures 15, 16, and 17 show the  $H\alpha$  velocities along PA 138, PA 150, and PA 179, respectively. Open circles and filled circles represent the results of multi-component Gaussian fittings and single Gaussian fittings, respectively. The latter represent intensity-weighted velocities of the  $H\alpha$  emission (section 3). The data along PA=134° taken from YKO11 are also plotted in Figure 15.

The velocity field of the total light  $H\alpha$  (blue points in Figures 15–17) is consistent with the previous works (McCarthy, Heckman & van Breugel 1987; Heckman, Armus & Miley 1990; Shopbell & Bland-Hawthorn 1998). The polarized  $H\alpha$  lines (red points in Figures 15–17) are systematically redshifted relative to the total light  $H\alpha$ . In addition, except for some regions on the SE side of the nucleus along PA 138 and PA 150, the polarized lines show higher velocity than the systemic velocity,  $v_{\text{sys}}$ , of M82. Assuming that the dust grains are acting as moving mirrors that scatter the light from the central region of the galaxy, we interpret that the polarized components whose velocities are higher than  $v_{\text{sys}}$  of the galaxy represent outflowing motion of the dust (YKO11). This tendency is

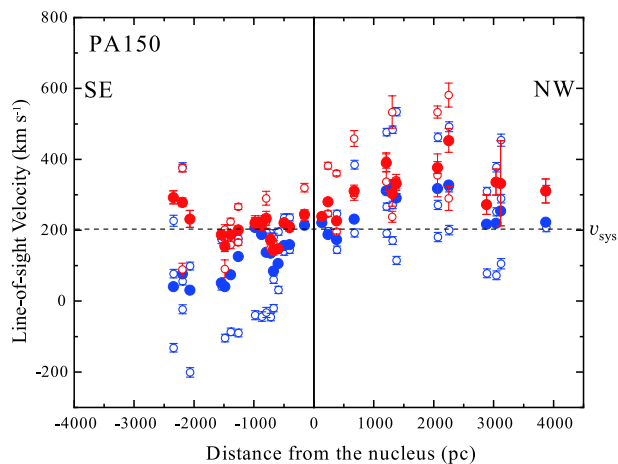


**Fig. 16.** The velocity field of the  $H\alpha$  emission lines along  $PA=150^\circ$ . Part of the data are taken from YK011.

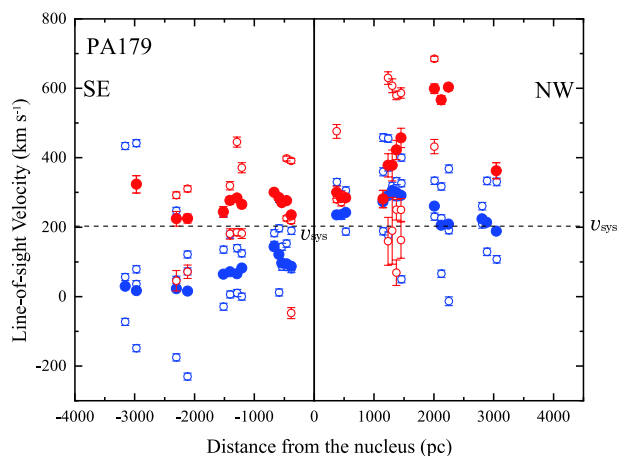


**Fig. 17.** The velocity field of the  $H\alpha$  emission lines along  $PA=179^\circ$ .

remarkable on the NW side of the nucleus. In particular, some data points on the NW side along PA 150 and PA 179 show significantly high velocities. The intensity-weighted velocity of the polarized emission line reaches as high as a  $500\text{--}600\text{ km s}^{-1}$  in these regions (Figures 16 and 17).

The intensity-weighted velocities of the polarized  $H\alpha$  for all PAs are summarized in Figure 18. The velocity field consists of three main components: outflow components seen on the NW and SE sides of the nucleus (“NW outflow” and “SE outflow”; Figure 18) and very low velocity component on the SE side (“VLV component”; Figure 18). The NW and SE outflows show accelerating velocity field with the distance. The scatter of the velocity fields of the outflows is as wide as a few hundreds  $\text{km s}^{-1}$  (e.g.,  $\simeq 300\text{ km s}^{-1}$  at  $\sim 2\text{ kpc}$  in the NW outflow), suggesting that there are multiple different kinematic components for the same distance in the outflows. The NW outflow is apparently faster than the SE outflow. Such asymmetric velocity field between the NW and SE sides can be ex-

plained by projection effect caused by the geometry and our viewing angle of a bi-conical outflow (see section 5.3). The VLV component seen along PA 138 and PA 150 is  $\sim 10\text{--}100\text{ km s}^{-1}$  slower than  $v_{\text{sys}}$ .

#### 4.2.2 Peculiar velocity components

There are several peculiar velocity components in the polarized  $H\alpha$  emission lines. Remarkable red wings in the polarized emission lines at 1–1.5 kpc NW along PA 138 (Figures 28 and 29 in Appendix 1) have velocities of  $\sim 700\text{ km s}^{-1}$  (Figure 15). The red wing is conspicuous at 1.31 kpc NW. The polarization degree reaches  $\sim 30\%$  for this component. The polarized  $H\alpha$  lines at 1.2–2.3 kpc NW along PA 179 also have strong red wing components (Figure 34 in Appendix 1). The velocities of these component reach  $\sim 600\text{ km s}^{-1}$  (Figure 17). At 2.19 kpc SE along PA 150, the polarized  $H\alpha$  line has a strong red peak and a broad blue wing in its profile (Figure 33 in Appendix 1). The polarization degree reaches  $\sim 60\%$  at the red peak, while it decreases down to  $\sim 10\%$  in the blue wing. The line-of-sight velocity of the red peak is  $\sim 400\text{ km s}^{-1}$ .

## 5 Discussion

### 5.1 Circumnuclear structure of M82 probed by scattering light

There are at least two main illumination sources that emit strong  $H\alpha$  emission in the nuclear region of M82. One of them is located around the  $2.2\text{ }\mu\text{m}$  stellar nucleus, whereas the other spatially corresponds to the radio 3 mm continuum and molecular gas concentration  $\sim 6''$  ( $\sim 100\text{ pc}$ ) west from the  $2.2\text{ }\mu\text{m}$  nucleus. The latter one is deeply embedded in the nuclear dust and cannot be seen in optical.

The fact that the outer dust scatters mostly light from the  $2.2\text{ }\mu\text{m}$  nucleus while the inner dust scatters light from the 3 mm peak suggests the following two possibilities: 1) inhomogeneous absorbing matter distribution produces different optical paths to the outer and inner regions from the central region of the galaxy, 2) the site of the active star formation has been changed from the  $2.2\text{ }\mu\text{m}$  source to the 3 mm source recently. The latter possibility has, however, a problem in timescale for changing the star formation sites. The boundary between the  $2.2\text{ }\mu\text{m}$  source reflecting region and the 3 mm source reflecting region is located around  $\sim 1\text{ kpc}$  from the nucleus, indicating that the transition timescale of the star forming site should be  $\sim 10^3\text{ yr}$  (the light traveling time from the center to the boundary) if the scenario 2) is the case. This timescale is much shorter than a typical timescale of star formation,  $\sim 10^7\text{--}8\text{ yr}$ , in starburst galaxies (Forster-Schreiber, Genzel

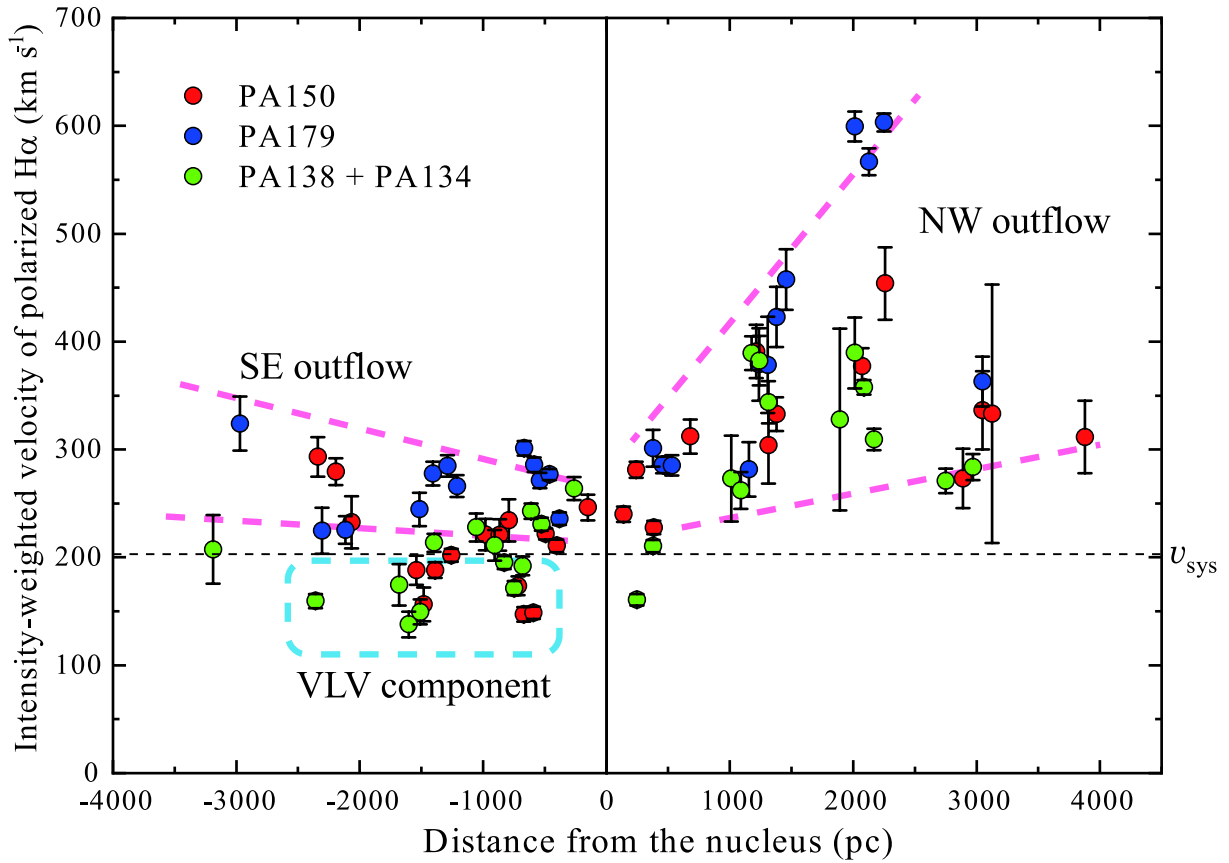


**Fig. 18.** The intensity-weighted velocity field of the polarized  $H\alpha$  emission lines of the superwind in M82. Red, blue, and green circles represent the data of  $PA=150^\circ$ ,  $179^\circ$ , and  $138^\circ$  and  $134^\circ$ , respectively. There seems to be a large scatter in the velocity field of the outflow. In addition, very low velocity (VLV) component whose velocity is smaller than the systemic velocity of the galaxy are seen along PA 138 and PA 150 on the SE side of the nucleus. This component is likely associated with the molecular gas stream rather than the outflow. See text for the detail.

& Lutz 2003).

The significant variations of the polarization angle within emission line profiles are seen in some regions near the nucleus, indicating that the scattered lights from different light sources are superposed at these regions (subsection 4.1). Interestingly, the M vectors of the blue components of P1 and P3 are directed to their nearby X-ray point sources (Figure 14), suggesting that the  $H\alpha$  emission from the vicinities of these sources is scattered by the dust located at these positions. The direction of the M vector of the blue component at P3 is slightly different from the direction to the bright X-ray source M82 X1. Taking dilution of the polarized light due to mixing of the blue and red components into account, the M vector of the intrinsic polarized light of the blue components could be directed very close to M82 X1. These X-ray sources have no counterparts in optical-infrared-radio wavelengths. They may be deeply embedded active compact objects surrounded by warm ionized gas. In fact, it is well known that ultraluminous X-ray sources like M82 X1 are often associated with optical emission line nebulae (Moon et al. 2011; Cseh et al.

2012). On the other hand, we cannot exclude the possibility that the blue components of P1 and P3 are scattered light from deeply obscured H II regions that are not related to the X-ray sources.

## 5.2 Molecular-gas stream and its effect on the polarimetry observations

Some part of the dust scattering the nuclear  $H\alpha$  emission is likely associated with the molecular gas “stream” that is kinetically separated from the outflow from the nucleus. To illustrate this, we overplot the polarization vectors on the CO map taken by Walter, Weiß & Scoville (2002) (Figure 19). They found that there are two kinetically distinct components in the molecular gas in the central region of M82; one of which is the outflow gas that is a part of the superwind and the other is the molecular gas stream which is likely associated with the H I gas stream extended between M82 and M81 (Yun, Ho & Lo 1993; Yun, Ho & Lo 1994; Chynoweth et al. 2008). Figure 19 shows that most of the positions of the SE side of PA 138 and several



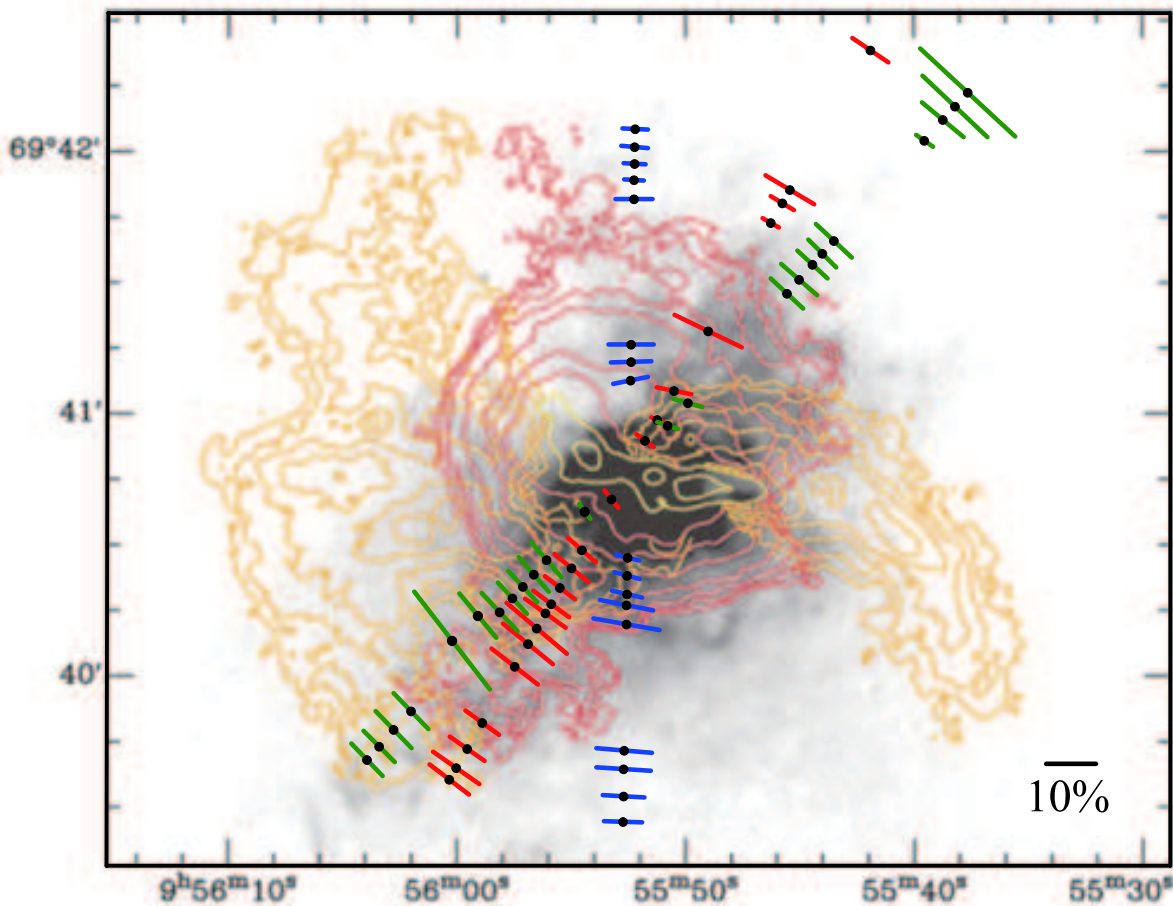


**Fig. 19.** The  $H\alpha$  polarization vectors overlotted on the CO  $J = 1-0$  map of M82 (Walter, Weiß & Scoville 2002). Most of the observed positions on the SE sides along both PA 138 (black dots with green colored polarized vectors) and PA 150 (black dots with red colored polarized vectors) are significantly overlapping on the molecular gas “stream” (yellow contours). On the other hand, the NW sides of the observed positions and the SE side along PA 179 (black dots with blue colored polarized vectors) are free from the molecular stream, and are spatially coincident with the “wind” component (red contours) of the molecular gas.

near-nucleus positions along PA 150 are located within the molecular gas stream (yellow contours in Figure 19). On the other hand, all the observed positions along PA 179 and the NW side of the nucleus along both PA 138 and PA 150 are spatially coincident with the molecular gas outflow (red contours in Figure 19). Because it is naturally expected that the molecular gas stream contains dusts, the dust kinematics probed by the polarized emission lines on the SE side of the nucleus along PA 138 and PA 150 are likely affected by the kinematics of the molecular gas stream. On the other hand, the polarized spectra on the NW side along all PAs, the SE side along PA 179, and the outer regions along PA 150 seem to follow the kinematics of the dust associated with the outflow.

The SE part of the molecular gas stream has almost zero or negative velocities relative to the systemic velocity of the galaxy (Walter et al. 2002). Salak et al. (2013) also decomposed the wind and stream components of the

extended molecular gas of M82 with their wide field CO map, and confirmed that the kinematics of the SE stream is dominated by transverse motion. These results are consistent with our results: the polarized  $H\alpha$  has lower velocity than the systemic one on the SE side along PA 138 and PA 150 (VLV component: Figure 18). YKO11 concluded that the dust is decelerated at  $\sim 1$  kpc. However, their observation was limited within  $\sim 1.5$  kpc SE from the nucleus along PA 134 and PA 150, where the molecular gas stream likely dominates. Therefore they sampled mostly the molecular gas stream component. We found that the dust outflow components, which are well probed by the polarized  $H\alpha$  on the NW side of the nucleus, are globally accelerated outwards (Figure 18). This work succeeds to discriminate the stream components from the global outflow components of the dust in the wind by much wider and deeper observations than those made by YKO11.

Recently, a very sensitive H I observation by Martini et

al. (2018) revealed that the neutral hydrogen gas is decelerated at  $\simeq 1$  kpc from the nucleus. This deceleration is more remarkable on the SE side than on the NW side. They suggested that the H I gas is decelerated by the drag force or interaction with ambient medium, and the decelerated gas will eventually fall back to the galaxy disk. However, they also pointed out a possibility that this apparent deceleration is due to chance overlap of the H I gas stream. The H I and CO streams and the VLV dust we found might be kinematically and spatially related. We suggest that the stream and outflow components are overlapping to each other in front of the SE wind.

### 5.3 Dust flow model

We constructed a toy model of the dust outflow to explain the velocity field of the polarized emission line (Figure 20). The main structure of the flow is bipolar hollowed cones, and the dust grains move along the walls of the cones. The basic assumptions are: 1) the dust grains act as moving mirrors reflecting the light from a light source, 2) the light source resides at the galaxy nucleus. The second assumption may be somewhat inconsistent with our discovery that there must be at least two light sources that illuminate the dust associated with the superwind. However, for simplicity, we adopted the above simple assumptions.

For astronomical dust scattering, the forward scattering is much more efficient than the backward scattering (e.g., van de Hulst 1957). Most of the polarized light thus comes from the forward scattering of the dust, i.e., the front side of the conical dust flow is dominant for the polarized emission lines. We note, however, that there are several regions where the polarized emission lines show conspicuous double peaked profile. Scattered light from both the front and back sides of the dust flow may be seen at those regions. In this work we utilize intensity-weighted velocities of the polarized emission lines for understanding the overall structure of the velocity field of the dust outflow.

The configuration of our toy model is shown in Figure 20 (YKO11; see also Appendix 3). We assume that the dust flow is launched just outside the central starburst region. Since the radius of the starburst region of M82 was estimated as  $\sim 300$  pc (Greve. 2004), we adopt this value as the cone base  $b$  (Figure 26 in Appendix 3). The opening angles of the outflow cone are different for different materials. For the warm and hot ionized gas, relatively narrow opening angles of  $\sim 5^\circ$ – $25^\circ$  have been proposed (Shopbell & Bland-Hawthorn 1998; Stevens, Read & Bravo-Guerrero 2003; Greve. 2004). On the other hand, wide ( $\sim 50^\circ$ – $90^\circ$ ) opening angles are suggested by infrared and radio observations (Alton, Davies & Bianchi 1999; Walter, Weiß &

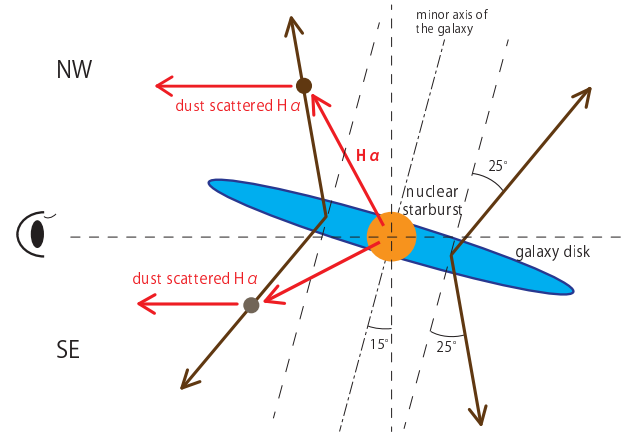


Fig. 20. The dust outflow model of the M82 superwind.

Scoville 2002; Engelbracht et al. 2006; Leeuw & Robson 2009; Kaneda et al. 2010; Leroy et al. 2015). Based on the above difference in morphology, we consider that a same flow configuration cannot be applied to the warm/hot outflow and the cold dust/molecular gas outflow. We thus adopt a wide opening angle of  $50^\circ$ , i.e., the  $1/2$  opening angle  $\theta = 25^\circ$  (see Figures 20 and 26 in Appendix 3), for our dust flow model. The inclination angle of the galaxy  $i = 15^\circ$  (Greve. 2004) is assumed. See YKO11 for the detailed discussion on our dust flow configuration. In addition, the position angle of the axis of the outflow cone is assumed to be  $PA = 156^\circ$ , from which we calculate the relative position angle  $\delta$  (Figure 27 in Appendix 3) of the slit.

The dust grains are accelerated outward due to radiation pressure from the central starburst region of M82. We assumed two cases for the dust distribution in the outflow: Case I: constant column density dust cloud case and Case II: mass conserved expanding shell case. These cases represent two extreme cases, and the real situation would be in between the two cases.

In Case I, the acceleration  $a$  to a dust cloud is proportional to inverse square of the distance  $l$ ;  $a \propto l^{-2}$ . The dust reaches a terminal velocity  $v_*$  at the infinite distance as

$$v_d(l) = v_* l_0^{1/2} (1/l_0 - 1/l)^{1/2}, \quad (1)$$

where  $v_d$  is the dust velocity at the distance  $l$  and  $l_0$  is the distance where the dust outflow is launched.

In Case II, the column density of the shell decreases as the shell expands, as  $l^{-2}$ , to conserve mass of the shell. In this case, both the radiation pressure and the column density decrease in the same manner as a function of the distance from the nucleus, so the acceleration is constant over both time and space. Therefore

$$v_d = at + v_0, \quad (2)$$

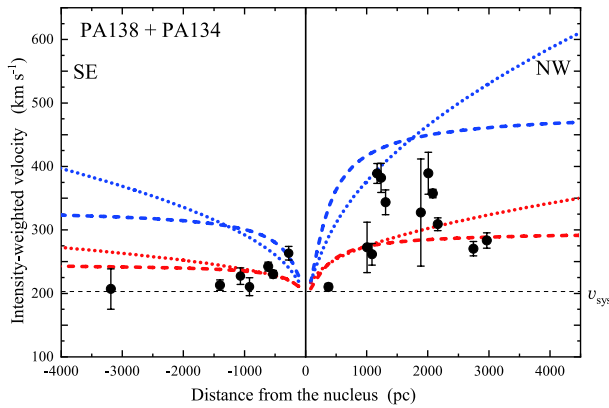


**Fig. 21.** Comparison between the observed polarized  $H\alpha$  velocity field along PA 138 with that of the dust wind models. Black dots represent the observation. We ignore the data points of the VLV component. Blue dashed and dotted lines represent the model loci of the HV-flows in Case I (constant column density dust cloud case) and Case II (mass conserved expanding shell case), respectively. Red dashed and dotted lines represents the model loci of the LV-flows in Case I and Case II, respectively. See text for the details.

where  $t$  and  $v_0$  are the time after the launch and the launch velocity along the cone, respectively. This velocity is also expressed as a function of distance  $l$  from the launch region in the disk as

$$v_d(l) = \sqrt{2al + v_0^2}. \quad (3)$$

The observed line-of-sight velocity within the outflow shows relatively large scatter for a given distance from the nucleus, spanning over 100–400  $\text{km s}^{-1}$  (Figure 18), suggesting that the wind consists of multiple kinematical subcomponents. We aim to represent the global characteristics by incorporating two kinematically distinct outflows; a high velocity flow with high acceleration, and low velocity flow with a moderate acceleration. We hereafter refer the former and latter as to “HV-flow” and “LV-flow”, respectively. For Case I, we adopt  $l_0 = 0.3$  kpc, and  $v_* = 300$   $\text{km s}^{-1}$  and  $v_* = 100$   $\text{km s}^{-1}$  for the HV- and LV-flows, respectively. For Case II, we adopt the acceleration  $a = 23$   $\text{km s}^{-1} \text{Myr}^{-1}$  and  $a = 2$   $\text{km s}^{-1} \text{Myr}^{-1}$  for the HV- and LV-flows, respectively. The launch velocity  $v_0$  is assumed to be 50  $\text{km s}^{-1}$  for both flows. For Case II, the HV-flow is accelerated to  $\sim 450$   $\text{km s}^{-1}$  and extends to  $l \sim 4$  kpc within  $\sim 10^7$  yr after the launch. The SV-flow is accelerated to  $\sim 150$   $\text{km s}^{-1}$  and extends to  $l \sim 4$  kpc within  $4 \times 10^7$  yr.

We compare the above model calculations with the intensity-weighted velocities of the polarized  $H\alpha$  emission line. The equation (A13) is used to calculate the observed line-of-sight velocity of the polarized  $H\alpha$  line from  $v_d(l)$  calculated with equations of (1) and (3). Figures 21–23 show the observed velocity and the HV- and SV-flows. We ignore the data points of the VLV component in the com-

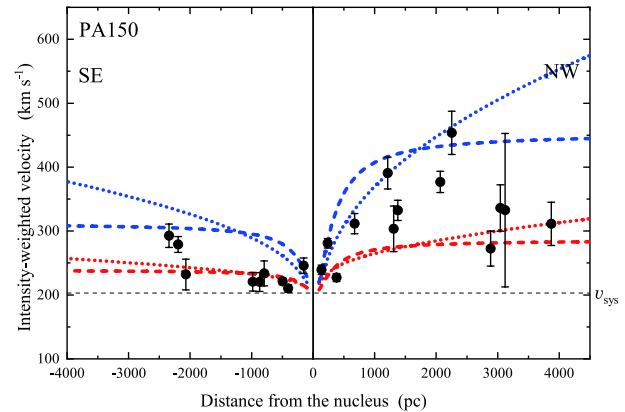


**Fig. 22.** Comparison between the observed polarized  $H\alpha$  velocity field along PA 150 with that of the dust wind models.

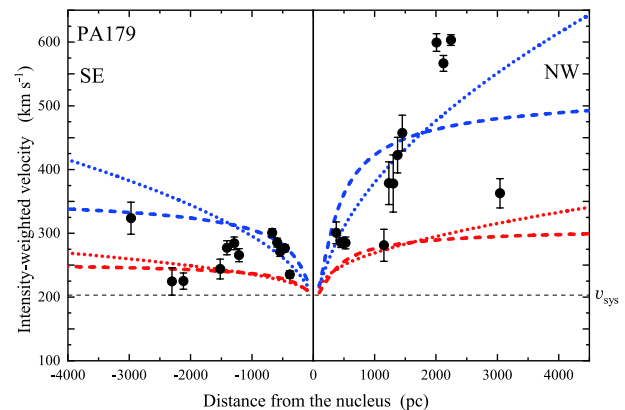


**Fig. 23.** Comparison between the observed polarized  $H\alpha$  velocity field along PA 179 with that of the dust wind models.

parison, because this component is likely associated with the molecular gas stream as discussed in subsection 5.2. The HV-flows seem to trace upper envelope of the observed velocity distribution of the polarized  $H\alpha$  line on the NW side of the nucleus along PA 150 (Figure 22) and PA 179 (Figure 23). It also traces the inner velocity field on the SE side of the nucleus along PA 179. The HV-flows, however, slightly overestimate the velocities at  $>1$  kpc on the SE sides of the nucleus along all PAs. The SV-flows well trace the lower envelope of the velocity distributions along all PAs (Figures 21–23). Although we cannot conclude which case, Case I or Case II, is more appropriate to reproduce the observations, it is clearly shown that some portion of the dust in the M82 superwind is accelerated to the velocity higher than  $\sim 300$   $\text{km s}^{-1}$ .

We here comment on a high-velocity red component of the polarized  $H\alpha$  line, whose line-of-sight velocity reaches  $\sim 500$   $\text{km s}^{-1}$  above the systemic velocity  $v_{\text{sys}}$ , at 1–1.5 kpc NW along PA 138 (Figure 15). Such redshifted components in double-peaked profile might come from back-scattered  $H\alpha$  emission by the dust residing on the back side

of the outflow cone. If this is the case, the HV-flow models can naturally reproduce such a redshifted component. The inclination angle of the backside of the flow is  $40^\circ$  on the NW side in our model configuration (Figure 20). The line-of-sight velocity of the back-scattered  $H\alpha$  emission is then calculated as  $\sim v_d(1 + \sin 40^\circ)$ , indicating that the dust flow whose velocity  $v_d$  is as high as  $\sim 300 \text{ km s}^{-1}$  at  $\sim 1 \text{ kpc}$  from the galaxy disk can explain the high velocity red component. This value of  $v_d$  is consistent with the HV-flow models both in Case I and Case II.

The kinematics of the outflowing dust derived in this work is globally consistent with recent numerical simulations of radiation pressure driven dusty winds performed by Zhang et al. (2018). They mainly investigated the behavior of dust clouds irradiated by strong radiation field. They found that the clouds are disrupted by the radiation pressure, and finally elongated along the direction of the motion. Some portion of the cloud acquires velocity as high as several hundreds  $\text{km s}^{-1}$ , leaving dense slow fragments behind. As a result, the cloud shows a large velocity dispersion of a few hundreds  $\text{km s}^{-1}$ . The mean velocity of the clouds reaches  $\sim 300\text{--}500 \text{ km s}^{-1}$  in  $10^6 \text{ yr}$  (Zhang et al. 2018), one order of magnitude shorter than that inferred from our toy models ( $\sim 10^7 \text{ yr}$ ). We note that their models assumed much luminous light source comparable to that of ultra-luminous infrared galaxies, which is a few orders of magnitude brighter than the nuclear starburst in M82.

#### 5.4 Luminosity of the scattered source

We estimated the  $H\alpha$  luminosity of the central light sources using the surface brightness (SB) of the polarized  $H\alpha$  emission line. We plot the SB of the total and the polarized  $H\alpha$  emission lines in Figure 24. The total light SB is proportional to  $l^{-3}$  out to 4 kpc. On the other hand, the polarized SB is roughly proportional to  $l^{-2}$  in the inner region, and it declines with steeper slope outside. Altogether, the total light SB declines steeper than the polarized SB within 1 kpc from the nucleus, whereas the latter declines steeper than the former at  $> 2 \text{ kpc}$ . We attributed the outer steeper decline of the polarized SB to absorption within the dusty wind, and we fitted the following model curve to the polarized SB,

$$SB_{H\alpha} = \frac{\eta F_{0,H\alpha}}{4\pi l^2} \exp(-\alpha l), \quad (4)$$

where  $SB_{H\alpha}$ ,  $F_{0,H\alpha}$ ,  $l$ , and  $\alpha$  are surface brightness of the polarized  $H\alpha$ ,  $H\alpha$  flux of the central light sources, distance from the central sources, and absorption coefficient, respectively. The scattering efficiency of the dust  $\eta$  represents the fraction of the light scattered toward the line-of-sight by

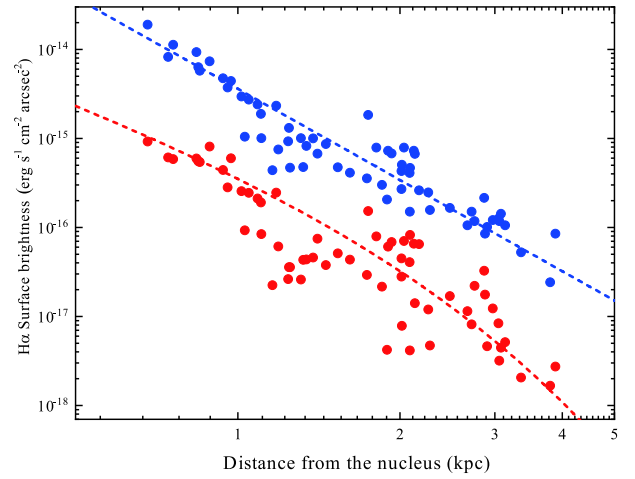


**Fig. 24.** Surface brightness distribution of the  $H\alpha$  emission line of M82. Blue and red points are the data of the total light and polarized light, respectively. The best fit model curve of single scattering plus constant optical depth for the polarized  $H\alpha$  is shown as a red dashed line. Blue dashed line is proportional to the negative cube of the distance ( $\propto l^{-3}$ ) representing well the trend of the  $H\alpha$  surface brightness of the total light.

dust. For simplicity, we assumed that  $\eta$  and  $\alpha$  are constant throughout the wind.

The best fitted model gives us  $\eta F_{0,H\alpha} = 1.2 \pm 0.2 \times 10^{-14} \text{ erg s}^{-1} \text{ cm}^{-2} \text{ arcsec}^{-2}$  and  $\alpha = 1.0 \pm 0.2 \text{ kpc}^{-1}$ . The  $H\alpha$  luminosity of the scattered sources is thus  $L_{H\alpha,ss} \sim 5 \times 10^{41} (\eta/0.1)^{-1} \text{ erg s}^{-1}$ . It is comparable to the total  $H\alpha$  luminosity of the M82 superwind (Shopbell & Bland-Hawthorn 1998);  $L_{H\alpha,wind} \sim 2.1 \times 10^{41} \text{ erg s}^{-1}$ . While the exact value of  $\eta$  is not known,  $L_{H\alpha,ss}$  could be an order of magnitude larger than the  $H\alpha$  luminosity of the central region of the nebula;  $L_{H\alpha,center} \sim 7 \times 10^{40} \text{ erg s}^{-1}$  (McCarthy, Heckman & van Breugel 1987). This suggests that a large fraction of the  $H\alpha$  emission is hidden from our direct line-of-sight due to strong extinction.

Assuming the true  $H\alpha$  luminosity is in an order of  $10^{42} \text{ erg s}^{-1}$ , we calculate the star formation rate (SFR) of the M82 starburst as  $\text{SFR} \sim 8 M_\odot \text{ yr}^{-1}$  using the  $L_{H\alpha}$ -SFR conversion equation proposed by Kennicutt (1998). This value is roughly consistent with the SFRs (9–13  $M_\odot \text{ yr}^{-1}$ ) of M82 derived based on infrared observations (e.g., Forster-Schreiber, Genzel & Lutz 2003; Strickland et al. 2004).

#### 5.5 Fate of the outflowing dust in the superwind of M82

Our kinematic model suggests that the dust associated with the superwind of M82 is accelerated outward from the nucleus; the outflow velocity of some portion of the dust in the wind reaches  $\sim 300\text{--}450 \text{ km s}^{-1}$  at  $\sim 4 \text{ kpc}$  from the nu-



cleus. This value is comparable to the range of the escape velocity of the galaxy ( $v_{\text{esc}} \sim 200\text{--}460 \text{ km s}^{-1}$ ; Strickland & Heckman 2009). A portion of the dust can thus be expelled from the galaxy disk and pollutes the halo of the galaxy and/or the intergalactic space. This picture is consistent with the results of infrared or submillimeter observations (Alton, Davies & Bianchi 1999; Engelbracht et al. 2006; Leeuw & Robson 2009; Kaneda et al. 2010; Contursi et al. 2013; Bierão et al. 2015), in which very extended ( $>$  a few kpc) dust emission around the galaxy is detected.

The huge amount of dust created in the starburst or residing in the galactic disk is exposed to the strong radiation pressure from the central starburst. Assuming that the dust and molecular gas are physically coupled, we expect that the molecular gas of M82 is dragged by the dust driven by the radiation pressure from the central starburst. However, the observed outflow velocity of the molecular gas ( $\sim 200 \text{ km s}^{-1}$ ; Salak et al. 2013; Leroy et al. 2015) is significantly lower than those of some parts of the dust outflow. The difference in kinematics between the dust and the molecular gas suggests that some fraction of the molecular gas is kinematically decoupled from the dust; i.e., a certain amount of the dust escapes from the galactic gravitational potential leaving the molecular gas in the galaxy. This seems to indicate that a part of the dust is selectively expelled from M82 to the galaxy halo and the intergalactic space. The extended dusty halo observed in mid-infrared (Engelbracht et al. 2006; Kaneda et al. 2010; Leroy et al. 2015), submillimeter (Alton, Davies & Bianchi 1999; Leeuw & Robson 2009), and UV (Hoopes et al. 2005) was possibly formed by this selective dust blown out mechanism. If this is the case, it can solve the apparent low Eddington ratio problem for the extended dusty halo pointed out by Coker et al. (2013) as well.

The kinematic difference between the dust flow and the warm ionized gas flow is also conspicuous. A number of works has derived that the warm ionized gas probed by  $\text{H}\alpha$  emission has an outflow velocity of  $\sim 600 \text{ km s}^{-1}$  (Heckman, Armus & Miley 1990; McKerith et al. 1995; Shopbell & Bland-Hawthorn 1998). The ionized gas seems to be rapidly accelerated near the nuclear region and reach its terminal velocity (McKerith et al. 1995). This kind of behavior is naturally expected from the Case I of our acceleration model, in which we assumed column density conserved dust accelerated by the radiation pressure of a central light source. However, the terminal velocity of the warm ionized gas ( $\sim 600 \text{ km s}^{-1}$ ) is much higher than that of the outflow dust ( $\sim 300\text{--}450 \text{ km s}^{-1}$ ). In addition, the outflow dust seems to have multiple kinematic components, which is suggested by numerical simulations (Zhang et al. 2018). We therefore suggest that the warm ionized

gas is also kinematically decoupled from the radiation pressured dust outflow. It may mean that the main mechanism of the warm ionized gas acceleration of the superwind of M82 is not the radiation pressure onto the dust grains in the entrained gas.

Leroy et al. (2015) found no large scale high velocity molecular and neutral gas outflow in M82. They concluded that the neutral materials mixed with dust return to the galaxy disk following fountain-like trajectories. The low velocity components of the dust flow found in this work may be physically coupled with these materials. Ohyama et al. (2002) proposed that there are wide angle dust flows near the galaxy disk based on the dust reddening in the disk of M82 (see also Ichikawa et al. 1994). These wide angle flows may be parts of the fountain-like flows of dust observed as the low velocity components of the dust flow. If this is the case, the dust outflow consists of at least two kinematically and geometrically different components; a cone-like high velocity dust outflow that will escape from the galaxy and a fountain-like low velocity component that will return to the disk.

A proposed configuration of the dust flows of M82 is schematically shown in Figure 25. Further observations such as spectropolarimetric two-dimensional mapping around the nuclear region of M82 would be needed to reveal the detailed structure of its dust outflow.

## 6 Conclusions

We performed deep spectropolarimetric observations of a prototypical starburst galaxy M82 with the Subaru Telescope in order to study the kinematics of the dust outflow. We obtained optical ( $\lambda\lambda = 6000\text{--}6800 \text{ \AA}$ ) polarized emission-line spectra out to  $\sim 4 \text{ kpc}$  far from the galaxy disk along three position angles,  $138^\circ$ ,  $150^\circ$  and  $179^\circ$ . The  $\text{H}\alpha$  emission line in the superwind is strongly polarized, and the polarization pattern shows dust scattering of the central light sources, consistent with the previous works. The polarization degree increases with the distance from the nucleus and reaches  $\sim 30\%$  at maximum. There are at least two light sources at the central region of the galaxy; one of which is located at the near-infrared nucleus and the other resides at one of the peaks of the 3 mm radio and molecular gas emission. The outer ( $> 1 \text{ kpc}$ ) dust is illuminated by the former, whereas the inner dust is scattering the light from the latter.

We investigated the dust motion from the velocity field of the polarized  $\text{H}\alpha$  emission line. The dust is accelerated outward on the NW side of the nucleus. At some regions on the SE side, in particular along PA 138, the dust has negative relative velocities with respect to  $v_{\text{sys}}$  indicating ap-



- Engelbracht, C. W. et al. 2006, *ApJL*, 642, L127
- Faucher-Giguère, C.-A., Quataert, E. & Hopkins, P. F. 2013, *MNRAS*, 433, 1970
- Ferrara, A., et al. 1991, *ApJ*, 381, 137
- Forster-Schreiber, N. M., Genzel, R. & Lutz, D. 2003, *ApJ*, 599, 193
- Fujita, A., et al. 2009, *ApJ*, 698, 693
- Ginard, D., et al. 2015, *A&A*, 578, A49
- Götz, M., et al. 1990, *A&A*, 240, 52
- Gputa, S., et al. 2016, *MNRAS*, 462, 4532
- Greve, A. 2004, *A&A*, 416, 67
- Heckman, T. M., Armus, L. & Miley, G. K. 1990, *ApJS*, 74, 833
- Heckman, T. M. et al. 2000, *ApJS*, 129, 493
- Heckman, T. M. 2003, *RevMexAA*, 17, 47
- Heckman, T. M., et al. 2015, *ApJ*, 809, 147
- Heckman, T. M. & Thompson, T. A. 2017, arXiv:1701.09062
- Hoopes, C. G. et al. 2005, *ApJL*, 619, L99
- Hopkins, P. F., Quataert, E. & Murray, N. 2012, *MNRAS*, 421, 3522
- Hughes, D. H., Gear, W. K & Robson, E. I. 1994, *MNRAS*, 270, 641
- Ichikawa, T., et al. 1994, *ApJ*, 433, 645
- Iye, M., et al. 2004, *PASJ*, 56, 381
- Kaaret, P., et al. 2001, *MNRAS*, 321, L29
- Kaaret, P., Ward, M. J., & Zezas, A. 2004, *MNRAS*, 351, L83
- Kaifu, N., et al. 2000, *PASJ*, 52, 1
- Kaneda et al. 2010, *A&A*, 514, A14
- Kashikawa, N., et al. 2002, *PASJ*, 54, 819
- Kawabata, K. S., et al. 1999, *PASP*, 111, 898
- Kawabata, K. S., et al. 2003, *SPIE*, 4841, 1219
- Kennicutt, Jr. R. C. 1998, *ARA&A*, 36, 189
- Kepley, A. A., et al. 2014, *ApJL*, 780, L13
- Krumholz, M. R. & Thompson, T. A. 2012, *ApJ*, 760, 155
- Krumholz, M. R. & Thompson, T. A. 2013, *MNRAS*, 434, 2329
- Lee, J. C., et al. 2009, *ApJ*, 706, 599
- Leeuw, L. L. & Robson, E. I. 2009, *AJ*, 137, 517
- Leroy, A. K., et al. 2015, *ApJ*, 814, 83
- Martin, C. L. 1998, *ApJ*, 506, 222
- Martin, C. L., Kobulnicky, H. A. & Heckman, T. M. 2002, *ApJ*, 574, 663
- Martin, C. L. 2005, *ApJ*, 621, 227
- Martin, C. L., et al. 2012, *ApJ*, 760, 127
- Martini, P., et al. 2018, *ApJ*, 856, 61
- Matsumoto, H., et al. 2001, *ApJL*, 547, L25
- Matsushita, S., et al. 2005, *ApJ*, 618, 712
- McCarthy, P. J., Heckman, T. M. & van Breugel, W. 1987, *AJ*, 92, 264
- McClow, M. -M., McCray, R. & Norman, M. L. 1989, *ApJ*, 337, 141
- McCourt, M., et al. 2015, *MNRAS*, 449, 2
- McKeith, C. D., Greve, A., Downes, D. & Prada, F. 1995, *A&A*, 293, 701
- Melioli, C., de Gouveia Dal Pino, E. M. & Geraissate, F. G. 2013, *MNRAS*, 430, 3235
- Moon, D. -S., et al. 2011, *ApJL*, 731, L32
- Murray, N., Ménard, B. & Thompson, T. A. 2011, *ApJ*, 735, 66
- Mutchler, M. et al. 2007, *PASP*, 119, 1
- Ohyama, Y. et al. 2002, *PASJ*, 54, 891
- Osterbrock, D. E. & Ferland, G. J. 2006, *Astrophysics of Gaseous Nebulae and Active Galactic Nuclei*, 2nd Ed. (Sausalito, CA: University Science Books)
- Ostriker, E. C. & Shetty, R. 2011, *ApJ*, 731, 41
- Peebles & Shankar 2011, *MNRAS*, 407, 2962
- Ranalli, P., et al. 2008, *MNRAS*, 386, 1464
- Roussel, H. et al. 2010, *A&A*, 518, L66
- Rubin, K. H., et al. 2014, *ApJ*, 794, 156
- Rupke, D. S., Veilleux, S. & Sanders, D. B. 2002, *ApJ*, 570, 588
- Rupke, D. S., Veilleux, S. & Sanders, D. B. 2005, *ApJS*, 160, 115
- Sakai, S. & Madore, B. F. 1999, *ApJ*, 526, 599
- Salak, D., et al. 2013, *PASJ*, 65, 66
- Salas, P., et al. 2014, *ApJ*, 797, 134
- Sanders, D. B. S., et al. 2003, *AJ*, 126, 1607
- Scarrott, S. M., Eaton, N. & Axon, D. J. 1991, *MNRAS*, 252, 12
- Schmidt, G. D., Angel, J. R. P. & Comwell, R. H. 1976, *ApJ*, 206, 888
- Schwartz, C. M. & Martin, C. L. 2004, *ApJ*, 610, 201
- Seaquist, E. R. & Clark, J. 2001, *ApJ*, 552, 133
- Seaquist, E. R., Lee, S. W. & Moriarty-Schieven, G. H. 2006, *ApJ*, 638, 148
- Shopbell, P. L. & Bland-Hawthorn, J. 1998, *ApJ*, 493, 129
- Socrates, A. & Sironi, L. 2013, *ApJL*, 772, L21
- Spitzer, L. Jr. 1978, *Physical Processes in the Interstellar Medium* (New York: Interscience)
- Stevens, I. R., Read, A. M. & Bravo-Guerrero, J. 2003, *MNRAS*, 343, L47
- Strickland, D. K. & Stevens, I. R. 2000, *MNRAS*, 314, 511
- Strickland, D. K., et al. 2004, *ApJS*, 151, 193
- Strickland, D. K. & Heckman, T. M. 2009, *ApJ*, 697, 2030
- Suchkov, A. A., et al. 1994, *ApJ*, 430, 511
- Telesco, C. M. et al. 1991, *ApJ*, 369, 135
- Tenorio-Tagle, G. & Muñoz-Tuñón 1998, *MNRAS*, 293, 299
- Thuma et al. 2000, *A&A*, 358, 65
- Thompson, T., et al. 2015, *MNRAS*, 449, 147
- Thompson, T. A. & Krumholz, M. R. 2016, *MNRAS*, 455, 334
- Tinbergen, J. 1996, *Astronomical Polarimetry* (New York: Cambridge University Press)
- Tsuru, T. G. et al. 2007, *PASJ*, 59, 269
- van de Hulst, H. C. 1957, *Light Scattering by Small Particles* (New York: J. Wiley & Sons)
- Veilleux, S., Cecil, G. & Bland-Hawthorn, J. 2005, *ARA&A*, 43, 769
- Veilleux, S., Rupke, D. S. N. & Swaters, R. 2009, *ApJL*, 700, L149
- Walter, F., Weiß, A. & Scoville, N. Z. 2002, *ApJL*, 580, L21
- Weiß, A., Walter, F. & Scoville, N. Z. 2005, *A&A*, 458, 533
- Westmoquette, W. S. et al. 2009, *ApJ*, 706, 1571
- Wills, K. A., et al. 1999, *MNRAS*, 309, 395
- Yamagishi, M., et al. 2012, *A&A*, 541, A10
- Yoshida, M., Kawabata, K. S. & Ohyama, Y. 2011, *PASJ*, 63, 493 (YKO11)

- Yun, M. S., Ho, P. T. P. & Lo, K. Y. 1993, ApJL, 411, L17  
Yun, M. S., Ho, P. T. P. & Lo, K. Y. 1994, Nature, 372, 530  
Zhang, D. & Davis, S. W. 2017, ApJ, 839, 54  
Zhang, D., et al. 2018, ApJ, 854, 110

### **Appendix 1 Spectropolarimetry data of the $H\alpha$ + $[N\ II]$ emission of M82**

The total light and polarized light spectra around  $H\alpha$ + $[N\ II]$  emission lines of the superwind in M82 are shown in Figures 28–36.

### **Appendix 2 Parameters of the polarized $H\alpha$ emission of M82**

The parameters of the polarized  $H\alpha$  emission of M82 derived in this work are summarized in Table 2.





$$v_{d,LS} = v_d (\sin \theta \cos \varphi \cos i \mp \cos \theta \sin i). \quad (\text{A12})$$

Using the above equations, we derive observed polarized velocity  $v_p$  as

$$v_p = v_d (\cos \Psi - \sin \theta \cos \varphi \cos i \pm \cos \theta \sin i) + v_{\text{sys}}, \quad (\text{A13})$$

where  $v_{\text{sys}}$  is the systemic velocity of the galaxy. In the above equations,  $\theta$ ,  $i$ , and  $b$  are constants, when the geometry of the cone model is fixed. We can derive  $\zeta$  from the observables  $\delta$  and  $d$  using the equations (A9), and  $\Psi$  and  $\cos \varphi$  using the equations (A2) and (A8). We then obtain the polarized velocity as a function of the observables ( $d$ ,  $\delta$ ) by the equation (A13).

**Table 2.** Parameters of the polarized H $\alpha$  emission line in the superwind of M82

PA	Dist. <sup>a</sup> kpc	Area <sup>b</sup> arcsec <sup>2</sup>	$f_{\text{H}\alpha,\text{t}}$ <sup>c</sup> 10 <sup>-17</sup> erg s <sup>-1</sup> cm <sup>-2</sup>	$v_{\text{t}}$ <sup>d</sup> km s <sup>-1</sup>	$f_{\text{H}\alpha,\text{p}}$ <sup>e</sup> 10 <sup>-17</sup> erg s <sup>-1</sup> cm <sup>-2</sup>	$v_{\text{p}}$ <sup>f</sup> km s <sup>-1</sup>	PD <sup>g</sup> %	Pol. PA <sup>h</sup> deg
138	2.97	7.6	92	287 ± 7	13	284 ± 23	14.1	46.4
	2.75	5.6	67	222 ± 7	13	271 ± 22	19.1	46.5
	2.17	3.0	78	252 ± 7	20	309 ± 20	26.1	47.3
	2.09	4.0	186	311 ± 6	34	358 ± 14	18.0	46.7
	2.01	2.3	63	296 ± 6	7	389 ± 36	10.9	50.1
	1.89	3.3	68	340 ± 7	3	328 ± 64	4.1	55.1
	1.31	4.0	189	266 ± 6	19	344 ± 28	10.0	47.2
	1.24	2.3	109	279 ± 6	9	382 ± 29	8.1	45.4
	1.18	3.0	224	259 ± 6	18	389 ± 23	8.2	47.3
	1.09	4.3	435	277 ± 6	42	262 ± 28	9.7	48.3
	1.01	2.3	242	284 ± 6	22	273 ± 41	9.0	47.7
	0.38	4.7	2381	190 ± 6	144	211 ± 12	6.1	74.3
	0.25	4.3	8317	173 ± 6	371	161 ± 11	4.5	72.5
	-0.53	3.0	1716	123 ± 6	163	231 ± 12	9.5	40.9
	-0.61	4.0	1884	118 ± 6	177	243 ± 14	9.4	41.2
	-0.68	2.0	589	108 ± 6	51	192 ± 18	8.6	42.8
	-0.75	3.7	880	100 ± 6	77	171 ± 13	8.8	42.7
	-0.83	3.3	772	111 ± 6	82	195 ± 13	10.6	43.8
	-1.40	6.0	471	68 ± 9	47	214 ± 17	10.1	44.4
	-1.51	3.3	225	62 ± 6	23	149 ± 22	10.5	44.8
-1.60	4.7	366	49 ± 6	33	138 ± 20	8.9	45.2	
-1.68	2.0	145	79 ± 6	13	175 ± 30	9.2	44.0	
-2.36	14.9	127	75 ± 7	30	160 ± 14	23.9	47.8	
-3.19	15.9	39	64 ± 6	12	207 ± 55	31.2	51.1	
150	3.88	6.3	54	224 ± 6	6	312 ± 34	11.4	59.5
	3.13	2.7	28	256 ± 7	3	333 ± 120	9.5	63.6
	3.05	4.0	47	220 ± 7	4	336 ± 36	8.1	62.0
	2.89	9.3	94	218 ± 7	7	273 ± 28	7.4	61.7
	2.26	5.3	83	328 ± 7	7	454 ± 34	8.8	56.7
	2.07	10.6	160	319 ± 7	14	377 ± 17	8.8	56.3
	1.38	1.7	112	292 ± 6	13	333 ± 16	11.4	58.7
	1.31	4.0	328	331 ± 6	18	304 ± 36	5.5	58.3
	1.22	4.3	567	312 ± 6	21	391 ± 25	3.8	60.0
	0.38	7.0	3658	175 ± 9	264	228 ± 6	7.2	78.6
	0.24	5.3	5144	189 ± 6	137	281 ± 7	2.7	70.0
	0.14	3.3	7100	223 ± 6	309	240 ± 7	4.4	53.9
	-0.40	3.7	2996	160 ± 9	224	211 ± 6	7.5	48.4
	-0.49	4.0	2515	158 ± 9	222	222 ± 7	8.8	49.8
	-0.59	4.3	1609	107 ± 9	122	149 ± 6	7.6	52.4
	-0.67	2.3	633	86 ± 11	57	147 ± 7	9.0	53.7
	-0.72	1.7	314	137 ± 11	32	174 ± 9	10.1	53.8
	-1.26	5.3	975	127 ± 9	82	202 ± 6	8.4	54.1
	-1.39	5.6	409	76 ± 9	35	188 ± 7	8.6	54.7
	-1.48	2.3	100	42 ± 9	11	156 ± 16	11.5	55.4
-1.54	2.7	109	52 ± 9	11	188 ± 14	10.0	52.9	
-2.07	3.0	45	32 ± 9	4	233 ± 24	10.0	57.2	
-2.19	7.6	164	78 ± 11	27	279 ± 12	16.7	56.8	

Table 2. (Continued)

PA	Dist. kpc	Area arcsec <sup>2</sup>	$f_{\text{H}\alpha,\text{t}}$ 10 <sup>-17</sup> erg s <sup>-1</sup> cm <sup>-2</sup>	$v_{\text{t}}$ km s <sup>-1</sup>	$f_{\text{H}\alpha,\text{p}}$ 10 <sup>-17</sup> erg s <sup>-1</sup> cm <sup>-2</sup>	$v_{\text{p}}$ km s <sup>-1</sup>	PD %	Pol. PA deg
	-2.34	5.0	62	42 ± 12	8	293 ± 18	13.2	57.6
179	3.05	9.0	128	189 ± 7	4	363 ± 32	3.2	87.2
	2.25	6.0	147	209 ± 7	9	603 ± 18	6.2	91.3
	2.13	4.3	290	206 ± 7	8	567 ± 23	2.9	86.6
	2.01	5.3	269	261 ± 7	13	599 ± 21	4.9	85.1
	1.46	3.0	258	292 ± 6	13	457 ± 31	5.1	86.7
	1.38	3.7	365	300 ± 7	20	423 ± 32	5.5	83.3
	1.31	2.3	233	306 ± 7	11	378 ± 35	4.6	86.7
	1.24	3.7	339	292 ± 7	14	379 ± 31	4.0	87.4
	1.15	3.3	146	273 ± 7	11	282 ± 34	7.4	89.9
	0.53	3.3	578	243 ± 6	53	285 ± 19	9.1	90.2
	0.46	3.0	505	236 ± 6	42	280 ± 15	8.3	91.6
	0.38	3.7	662	236 ± 6	47	308 ± 26	7.1	101.8
	-0.38	2.3	4402	88 ± 6	215	236 ± 12	4.9	74.7
	-0.46	4.3	4855	95 ± 6	263	277 ± 10	5.4	73.9
	-0.54	2.3	2167	98 ± 6	139	271 ± 14	6.4	76.0
	-0.59	1.7	1221	122 ± 6	135	286 ± 13	11.0	78.1
	-0.67	5.3	2342	144 ± 6	318	301 ± 12	13.6	80.0
	-1.21	1.7	79	83 ± 7	9	266 ± 18	11.2	84.9
	-1.29	5.0	205	66 ± 7	23	285 ± 18	11.1	85.9
	-1.41	5.0	177	72 ± 7	15	278 ± 19	8.4	86.0
	-1.52	4.3	130	65 ± 7	10	244 ± 26	7.8	87.9
	-2.12	7.6	127	16 ± 7	14	225 ± 20	10.8	87.0
	-2.30	8.3	88	24 ± 7	12	225 ± 27	13.9	90.0
	-2.97	9.3	49	18 ± 8	5	324 ± 21	10.2	90.5

a. Distance from the nucleus. NW is positive and SE is negative.

b. Flux integration area.

c. Flux of total H $\alpha$  emission.

d. Intensity-weighted radial velocity of the total H $\alpha$  emission.

e. Flux of polarized H $\alpha$  emission.

f. Intensity-weighted radial velocity of the polarized H $\alpha$  emission.

g. Degree of polarization of the H $\alpha$  emission line.

h. Intensity-weighted position angle of polarization.